Optical photometry of two transitional millisecond pulsars in the radio pulsar state

James G. Stringer, Rene P. Breton, Colin J. Clark, Guillaume Voisin, Mark R. Kennedy, Daniel Mata Sànchez, Tariq Shahbaz, Vik S. Dhillon, Marten van Kerkwijk, Tom R. Marsh

Monthly Notices of the ROYAL ASTRONOMICAL SOCIETY

MNRAS **507,** 2174–2191 (2021) https://doi.org/10.1093/mnras/stab2167
Advance Access publication 2021 July 28

Optical photometry of two transitional millisecond pulsars in the radio pulsar state

J. G. Stringer [1★] R. P. Breton [1★] C. J. Clark [1,2,3] G. Voisin [1,4] M. R. Kennedy [1] D. Mata Sánchez,[1,5,6] T. Shahbaz,[5] V. S. Dhillon [7] M. van Kerkwijk[8] and T. R. Marsh[9]

[1]*Department of Physics and Astronomy, Jodrell Bank Centre for Astrophysics, The University of Manchester, Manchester, M19 9PL, UK*
[2]*Max Planck Institute for Gravitational Physics (Albert Einstein Institute), Hannover, Callinstraße 38, D-30167 Hannover, Germany*
[3]*Leibniz Universität Hannover, D-30167 Hannover, Germany*
[4]*LUTH, Observatoire de Paris, PSL Research University, 5 Place Jules Janssen, F-92195 Meudon, France*
[5]*Instituto de Astrofísica de Canarias, Vía Láctea, E-38205 La Laguna, Tenerife, Spain*
[6]*Departamento de Astrofísica, Universidad de La Laguna, E-38206 La Laguna, Tenerife, Spain*
[7]*Department of Physics and Astronomy, The University of Sheffield, Western Bank, Sheffield S10 2TN, UK*
[8]*Department of Astronomy & Astrophysics, University of Toronto, 50 St. George Street, Toronto, M5S 3H4 Ontario, Canada*
[9]*Department of Physics, The University of Warwick, Coventry, West Midlands CV4 7AL, UK*

Accepted 2021 July 12. Received 2021 June 17; in original form 2021 April 12

ABSTRACT

We present ULTRACAM multiband optical photometry of two transitional millisecond pulsars (tMSPs), PSR J1023+0038 and PSR J1227−4853, taken while both were in their radio pulsar states. The light curves show significant asymmetry about the flux maxima in all observed bands, suggesting an asymmetric source of heating in the system. We model the light curves using the ICARUS binary code, using models with an additional 'hotspot' heating contribution and an anisotropic heat redistribution model to treat the asymmetry. Our modelling reveals companion stars with underfilled Roche lobes in both PSRs J1023+0038 and J1227−4853, with Roche lobe filling factors in the range $f \sim 0.82-0.92$. While the volume-averaged filling factors are closer to unity, significant underfilling is unexpected from tMSPs as they must rapidly overfill their Roche lobes to start transferring mass, which occurs on time-scale of weeks or months. We discuss the motivation and validity of our extensions to the models and the implications of the underfilled Roche lobe, and suggest future work to further investigate the role of the filling factor in the tMSP cycle.

Key words: binaries: close – stars: evolution – stars: neutron – pulsars: individual: PSR J1023+0038 – pulsars: individual: PSR J1227−4853.

1 INTRODUCTION

1.1 Spiders and transitional millisecond pulsars

Transitional millisecond pulsars (tMSPs) are a class of neutron star binary containing a recycled millisecond pulsar (MSP), spun up by accretion from a low-mass semidegenerate companion to spin periods of the order of milliseconds (Alpar et al. 1982). tMSPs are unique in that they are observed to transition between an accretion-powered (AP) low-mass x-ray binary (LMXB) state and a rotation-powered (RP) radio pulsar state, the latter so far associated with the 'redback' class of pulsars (Archibald et al. 2009). Redbacks are a sub-class of the eclipsing 'spider' binaries in which a low-mass ($0.2\,M_\odot \lesssim M_c \lesssim 0.4\,M_\odot$) quasi-main sequence companion star in a tight (∼few hour) tidally locked orbit is irradiated by the wind of an MSP. This results in the ablation of the companion's surface into a tail of ionized matter, causing long eclipses at radio frequencies, and distinctive quasi-sinusoidal optical modulation caused by heating of the inner face of the companion, e.g. Breton et al. (2013); Roberts (2011). Spider binaries host some of the most massive and fastest spinning neutron stars (Linares 2020).

As summarized in Britt et al. (2017), observations of the three confirmed tMSP systems have revealed several shared characteristics, though it is important to note that due to the small sample size these could be coincidental. The optical emission in the RP state is indistinguishable from that of non-tMSP redback systems as described in the previous paragraph, while the AP state emission exhibits bimodal flickering and flaring (Kennedy et al. 2018; Shahbaz et al. 2018). In the AP state, bimodal flickering and flaring is also visible in the X-ray, which indicates that an accretion disc is present (Linares 2014; Patruno et al. 2014; Bogdanov et al. 2015). This is further confirmed by the strong emission lines in the optical spectrum seen in the AP state (Archibald et al. 2009; Bassa et al. 2014; Coti Zelati et al. 2014) which fully disappear in the RP state. In the AP state, tMSPs exhibit a flat radio spectrum suggesting self-absorbed synchrotron emission (Deller et al. 2015; Bogdanov et al. 2018), while in the RP state the radio emission is pulsed with a spectrum characteristic of synchrotron emission with a steep power law (Archibald et al. 2009; Patruno et al. 2014), typical of RP MSPs.

★ E-mail: james.stringer@postgrad.manchester.ac.uk (JGS); rene.breton@manchester.ac.uk (RPB)

1.2 The tMSP–LMXB link

tMSPs present a unique opportunity to not only study the accretion mechanism of LMXBs, but also gain insight into the evolution of pulsar binary systems. It is generally agreed that LMXBs are the predecessor to spiders and several other types of MSP binary, but the mechanism by which the accretion is 'switched off' is not known (Chen et al. 2013), nor is the mechanism by which the MSP magnetic field decays as it gets recycled (Konar & Bhattacharya 1997; Cumming, Zweibel & Bildsten 2001). As such, the study of tMSPs is important in uncovering the evolutionary history of spiders and LMXBs: they may be a missing link between these two populations (Archibald et al. 2009; Papitto et al. 2013). However, it is possible that they are themselves a distinct population; in this case they remain important astrophysical laboratories to study the accretion process. Since the time-scale of their transitions is on the order of weeks or months, with transitions occurring every few years, we can study the entire accretion process on human time-scales.

We present new optical light curves of two tMSPs, both in the radio pulsar states: PSRs J1023+0038 and J1227−4853. These are two of the three confirmed tMSPs; the third is PSR J1824−2452I, although its location in a globular cluster prevents a detailed study in optical wavelengths (De Falco et al. 2017; Coti Zelati et al. 2019). We note that there are a few 'candidate' tMSPs, such as 3FGL J0427.9−6704 (Strader et al. 2016; Kennedy et al. 2020), which show similar AP state properties to confirmed tMSPs but lack a radio MSP association and have not yet been seen to transition.

1.3 PSR J1023+0038

Often referred to as the canonical tMSP, PSR J1023+0038 (hereafter J1023) was initially classified in 2001 as a cataclysmic variable system with a binary period of 0.198 d (4.75 h; Bond et al. 2002). The double-peaked emission lines and blue optical spectrum indicated an accreting binary with a white dwarf primary, with optical photometry showing the flickering and flaring typical of an accretion disc. Woudt, Warner & Pretorius (2004) and Thorstensen & Armstrong (2005) presented the first evidence for a state change, respectively showing optical photometry and spectroscopy which lacked the usual signatures of an accretion disc. The strong emission lines in the optical spectra were replaced by absorption features, while the flickering and flaring in the light curve were no longer present. The state change was confirmed in 2007 with the detection of a radio pulsar with a spin period of 1.69 ms (Archibald et al. 2009; Wang et al. 2009).

In June 2013, the radio pulsations from the MSP could no longer be observed (Stappers et al. 2014), and were replaced by rapidly varying X-ray flux (Patruno et al. 2014) and optical signatures (Coti Zelati et al. 2014; Takata et al. 2014) indicative of an accretion disc. Kepler-K2 optical observations in 2017 further show clear evidence of an accretion disc with the slightly asymmetric, sinusoidal orbital light-curve modulation still visible (Kennedy et al. 2018; Papitto et al. 2018). J1023 displays several further characteristics not yet seen in other tMSPs. Ambrosino et al. (2017) report observations of optical pulsations of J1023 in its AP state, originating from inside the magnetosphere, and the flickering behaviour seen in the AP state is observed to occur simultaneously in optical and X-ray wavelengths (Papitto et al. 2019). Near-infrared flaring is also seen (Baglio et al. 2019). Lastly, pulsed X-ray and UV emission has been detected (Jaodand et al. 2016, 2021).

1.4 PSR J1227−4853

Identified as a variable X-ray source with *XMM-Newton* (Bonnet-Bidaud et al. 2012; de Martino et al. 2013), XSS J12270−4859 (now PSR J1227−4853, hereafter J1227) was initially classified as an LMXB due to the presence of flares and 'dips' in the X-ray light curve. Between 2012 and 2013, the X-ray and optical fluxes of J1227 were observed to decrease to new minima (Bassa et al. 2014; Bogdanov et al. 2014), and the spectral emission features of an accretion disc disappeared. Radio observations revealed an MSP with a period of 1.69 ms at the source coordinates (Roy et al. 2015), showing that J1227 had transitioned from an LMXB state to radio pulsar state displaying a redback-like optical modulation with an orbital period of 0.288 d (6.91 h). Gamma ray pulsations at the radio MSP period were discovered using data from the Large Area Telescope (LAT) on the *Fermi Gamma-ray Space Telescope* (*Fermi*-LAT), which indicated an LMXB to a tMSP transition epoch of 2012 November 03 (Johnson et al. 2015).

1.5 Summary of this work

In this study we first present our new photometry, outlining the reduction and calibration procedure, in Section 2. In Section 3 we discuss the nature of and the potential mechanisms behind the asymmetry of the light curves. We discuss our modelling of these light curves using the ICARUS binary light curve synthesis code in Section 4, in particular our constraints on the orbital parameters of the systems, and implement two extensions to the ICARUS model. The first extension accounts for an additional hotspot on the surface of the companion, and the second is a new description of the temperature distribution of the companion which takes into account diffusion and convection in the outer shell. Then, we outline the results of the modelling and discuss their validity and the implications on the tMSP transition mechanism in Sections 5 and 6.

2 OPTICAL OBSERVATIONS

2.1 ULTRACAM on the NTT

Our observations were performed using the ULTRACAM instrument mounted on the 3.5 m New Technology Telescope (NTT) at the La Silla observatory, Chile. ULTRACAM (Dhillon et al. 2007) is an optical imaging photometer capable of simultaneous three band observation. We used filters from the ULTRACAM Super Sloan Digital Sky Survey (Super-SDSS) u_s, g_s, r_s, i_s, z_s photometric system (Dhillon et al. 2018), with u_s and g_s filters on the first two CCDs, and either of i_s or z_s for the third. Our typical integration time was 10 s with 25 ms dead time between each frame. Our observations are summarized in Table 1.

2.2 Observations of J1227

J1227 was observed on 2019 February 27 beginning at 03:09:53 UTC, during its radio pulsar state. The observations were completed in one night, providing more than 90 per cent orbital phase coverage in mostly photometric conditions, although some clouds were present near the end of the observation, decreasing the signal-to-noise ratio (SNR) of these images. We reduced the data with the ULTRACAM pipeline using an ensemble aperture photometry method (Honeycutt 1992). We used eight comparison stars common to u_s, g_s, and i_s to correct for atmospheric transmission variations. We employed the same eight calibration stars of known i_s and g_s magnitudes from

Table 1. Table of observations of J1227 and J1023, with information gathered from the ULTRACAM online logs and reduction files. The seeing, displayed as the median, was calculated from the full width at half-maximum of the observations. Both nights used the u_s / g_s / i_s configuration of filters; the number of exposures in the table correspond to these filters. Further to the co-adds shown here, no further binning in time was performed during reduction.

Date	Start time (UTC)	Source	Exposures	Phase coverage	Seeing (')	Airmass	u_s co-adds time (s)	Exposure
2010 May 04	23:03:48	J1023	1859 / 1858 / 102	∼105 per cent	1.23	1.15–2.08	18	9.56
2019 Feb 27	03:04:41	J1227	2360 / 2359 / 1180	∼90 per cent	0.90	1.06–1.42	2	10.02

the AAVSO Photometric All-Sky Survey (APASS) to calibrate the i_s and g_s magnitudes to the absolute photometry system.[1] The same comparative photometry was also performed for the u_s-band, but as there were no objects with known u_s magnitude in the field we used the zero-point of this band, calculated from separate observations of SDSS standard stars, to calibrate the magnitudes instead. While the zero-point and typical extinction coefficients are known for ULTRACAM in this configuration, this is a less accurate calibration method than comparative photometry, so we included a larger band calibration offset for the *u'*-band in the modelling.

During observations a temporal co-addition factor of 2, where the CCD is read out every other exposure, was used for the u_s-band and the resulting SNR of the data was sufficient that we did not need to perform any further temporal averaging of any of the bands. The final step of our reduction was to discard any observations with error flags from the pipeline or SNR below a threshold of 3. This second condition was used as several observations near the optical minimum were impacted by cloud cover. The resulting data set contains a total of 5899 good data points: 2360 in i_s, 2359 in g_s, and 1180 in u_s. These data were folded at the orbital period using the ephemerides from radio timing (Roy et al. 2015). We will apply the following convention throughout the paper to define the orbital phase: phase 0.0 corresponds to the pulsar ascending node (i.e. for a circular orbit, this is defined as the quadrature point when the pulsar is moving away from us), with the companion's inferior conjunction (optical minimum) occurring at phase 0.25.

The phased light curve of J1227 (see Fig. 1) displays single-peaked sinusoidal modulation due to the irradiation of the companion. The peak-to-peak amplitude of modulation is approximately 0.6 mag in i_s, 0.8 mag in g_s, and 1.4 mag in u_s, with mean magnitudes of 18.0, 18.7, and 20.4 mag, respectively. Considering the colour information, the companion star becomes redder during the pulsar superior conjunction (optical minimum), in line with the expectation that the night side of the star is cooler than the day side. The light curve shows the asymmetric nature of the modulation, and a 'flattening' of the optical maxima most noticeable in the *i'*-band due to a significant ellipsoidal modulation contribution.

2.3 Observations of J1023

J1023 was observed over three consecutive nights starting on 2010 May 04, during the object's radio pulsar state. While the observations provide nearly 100 per cent phase coverage in u_s, g_s, i_s, and z_s, the latter two nights suffered from cloudy skies and so the quality of the first night of observations far exceeds that of the second and third, both in terms of usable phase coverage and SNR. Additionally, due to the cloud cover, the magnitude calibration is not completely

[1] https://www.aavso.org/apass

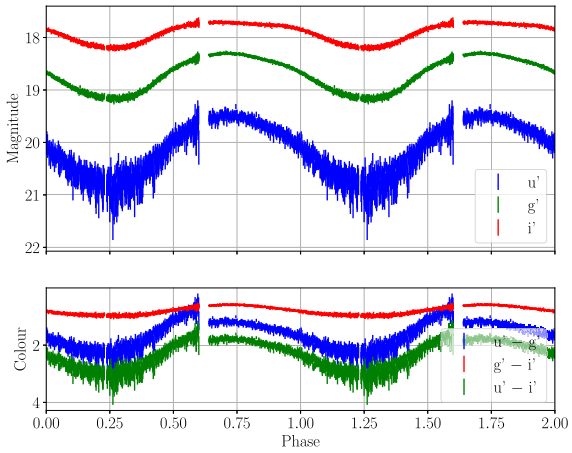

Figure 1. Phased light curve of J1227, repeated over two cycles for clarity, with each colour corresponding to a different filter as in the legend. The asymmetry can clearly be seen in the i_s and g_s bands around phase 0.75. At phase 0.6, the Sun rising is responsible for the large scatter, particularly so in the u_s-band. The bottom panel shows the colour information. We adopt the phase convention where the pulsar is at superior conjunction at phase 0.25.

consistent between nights. As such, we performed the modelling using just the data from 2010 May 04 to ensure that these potential calibration issues did not affect the results.

The observations were reduced in the same way as with J1227, using ensemble aperture photometry with the ULTRACAM pipeline. However, as the position of J1023 has been covered by the SDSS, calibration stars were available for all four bands, including *u'*. In total, 12 comparison stars were used for i_s and z_s, 11 for g_s, and 6 for u_s, with the same number being used to calibrate the magnitudes. We obtained a total of 3819 good data points; 1859 in i_s, 1858 in g_s, and 102 in u_s, which were folded on the orbital period.

The phased light curve, shown in Fig. 2 shows asymmetrical modulation in all three bands, with a single irradiation peak in u_s. The relative contribution of the ellipsoidal variation to the light-curve shape, which produces the double-peaked modulation per orbit (see e.g. Li, Halpern & Thorstensen 2014 for a clear example of this), is higher for redder bands (see e.g. i_s-band compared to u_s-band). We measure mean magnitudes of 17.3 in i_s, 17.9 in g_s, and 19.4 in u_s, with modulation amplitudes of 0.3, 0.4, and 0.7 mag, respectively.

2.4 Radial velocities

To help constrain the projected companion radial velocity, K_2, of J1023 we combined our photometric data with spectroscopic radial velocity measurements from Shahbaz et al. (2019) and McConnell et al. (2015). We used radial velocity curves obtained from metallic line spectra captured with the ISIS instrument on the 4.2 m William

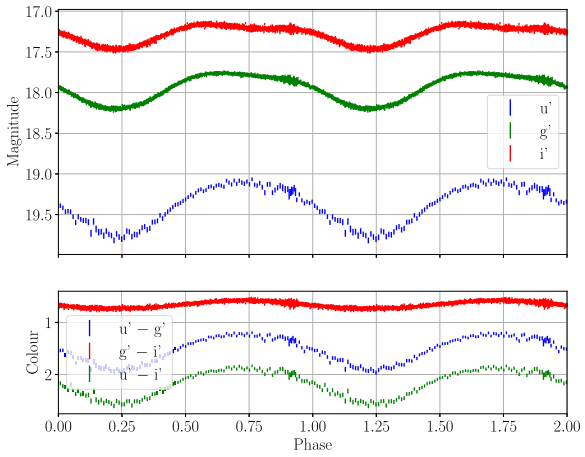

Figure 2. Phased light curve of J1023, clearly showing the asymmetry around phase 0.75. Similarly to J1227, this asymmetry is more pronounced in the i_s and g_s-bands. Note that the artefacts around phase 0.8–0.9 are due to poor seeing conditions.

Herschel Telescope in 2016 for Shahbaz et al. (2019) and 2009 for McConnell et al. (2015). Both radial velocity curves had been produced using broadly the same set of metallic lines, over the same range of wavelengths.

3 ASYMMETRIES

While observed in both these tMSP systems, asymmetric light curves appear to be a feature of redback systems in general (e.g. PSR J2215+5135; Schroeder & Halpern 2014) and are not specific to tMSPs. They are also not unique to either the RP state or AP state of a tMSP, as the asymmetry visible in the optical light curve of J1023 presented in this work during the RP state is also visible during the AP state (Kennedy et al. 2018; Papitto et al. 2018). As such, it is unlikely that they arise from, for example, reprocessing or obscuring of the pulsar wind by some disc remnant. Indeed there is no mechanism driving the asymmetry that is widely accepted and evidenced, though there are a number of possible theories.

Considering the work of Romani & Sanchez (2016), a swept-back intra-binary shock (IBS) between the pulsar and companion winds could be responsible for the asymmetry via heating of the companion by non-thermal X-ray emission produced in the wind shock. In their work, the modelling includes the effect of the IBS heating on the companion and finds good agreement with data. More recently, Kandel et al. (2020) performed modelling of the asymmetric redback PSR J2339−0533 using a hotspot model which aims to describe the ducting of high-energy particles (such as those shed from the IBS) on to magnetic caps on the companion star's surface.

Despite the relative success of the models linked to the IBS, the results of Zilles et al. (2020), which estimate the penetration depths of high-energy photons in the companion photosphere, suggest that the X-rays reprocessed by the shock could not sufficiently heat the companion to the observed asymmetry temperatures.

Dynamics on the companion surface may instead produce an asymmetric temperature profile. As the day side of the companion is strongly heated, we may expect strong circulatory winds and thermal structures similar to those observed on hot Jupiters (see e.g. Jackson et al. 2019; Komacek & Showman 2020) or cataclysmic variables (CVs; Martin & Davey 1995). The lack of fusion in hot Jupiters allows these global winds to form complex meteorologies, which are unlikely to form on redback companions as the radial convection in the envelope would disrupt it. The large temperature gradient between the day and night side would be sufficient to fuel the winds and so allow heat to flow through the atmosphere with circulation driven by the spin of the companion. We implement this as presented in Voisin et al. (2020); however, we note there are possible alternatives. In de Wit et al. (2012), an alternative hotspot model is presented with the temperature distribution motivated by these thermal flows. Or, in Demory et al. (2013), a longitudinal temperature map of the surface of the companion is used, using a number of fixed bands.

A recent novel approach in Romani et al. (2021) models the asymmetry of the optical light curve of the black widow pulsar PSR J1810+1744 by acting on the gravity darkening parameter. However, this method was used in the case of a very highly irradiated companion, while these tMSPs display only modest irradiation compared to their internal energy output.

We note the similarity to the HW Vir class of compact binaries, consisting of a hot sub-dwarf primary and cool close companion (typically a white dwarf; Schaffenroth et al. 2019), which do not display asymmetric light curves despite the otherwise similar orbital parameters. In these systems the sub-stellar point on the companion is heated to temperatures of over $\sim 10^4$ K, significantly more than the tMSPs in this work. We suggest that the depth to which the irradiation penetrates the companion's photosphere in HW Vir binaries is significantly shallower than with tMSPs due to the different source of heating. As such, the heat redistribution layer may not be sufficiently deep to produce asymmetries.

To illustrate the asymmetry in J1023, we overlay the light curves of each band, in fluxes, over the same light curve mirrored about phase 0.5. We are then able to analyse the asymmetry by calculating the residuals. We normalize these residuals to the mean flux of each band, then interpolate the flipped light curve at the phases of the original in order to calculate residuals between each curve. Note that this means that these are not residuals in the traditional sense due the interpolation; however, they clearly demonstrate the difference between the original and mirrored light curves. Seen in Fig. 3, the residuals follow a nearly sinusoidal shape across all three bands. The amplitude of these sinusoids is also comparable across the bands, largest in the g_s-band, followed closely by i_s, and then u_s at around 60 per cent the amplitude of i_s. Note that there is significantly increased scatter in u_s compared to g_s and i_s, which causes the amplitude of the sinusoid to appear larger than it is.

Performing the same analysis on the light curves of J1227, we find that the shape of the residuals is again consistent between each band. However, they more closely follow the shape of a sinusoid at the second harmonic; this is shown in Fig. 4 for the g_s-band. Additionally, the amplitude of this modulation is much more varied between bands; strongest in u_s, decreasing to 60 per cent in g_s, and finally, to roughly 25 per cent in i_s.

4 NUMERICAL MODELLING

4.1 ICARUS

We modelled our optical light curves using the ICARUS code (see Breton et al. 2012 for a thorough introduction) in order to constrain the orbital parameters of the system and the temperature profile of the irradiated companion. We use atmosphere grids created using the ATLAS9 synthesis code (Castelli & Kurucz 2003). In the standard heating model, the input parameters the model uses are as follows: the orbital inclination angle, cos (*i*); the Roche lobe (RL) filling factor, *f*; the base (night side) temperature of the companion, T_0; the irradiation

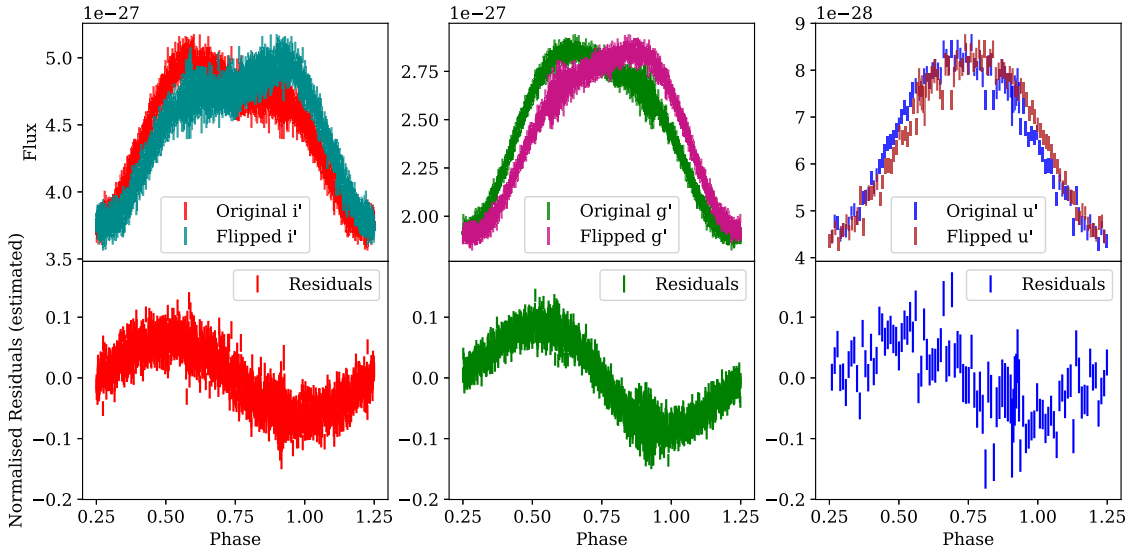

Figure 3. Top: i_s, g_s, and u_s light curves of J1023 overlaid with the same light curves mirrored about phase 0.5, illustrating the asymmetries. Bottom: estimated residuals between original and mirrored light curves, normalized to the mean band flux. The mirrored light curve was interpolated over the original phases in order to calculate these residuals.

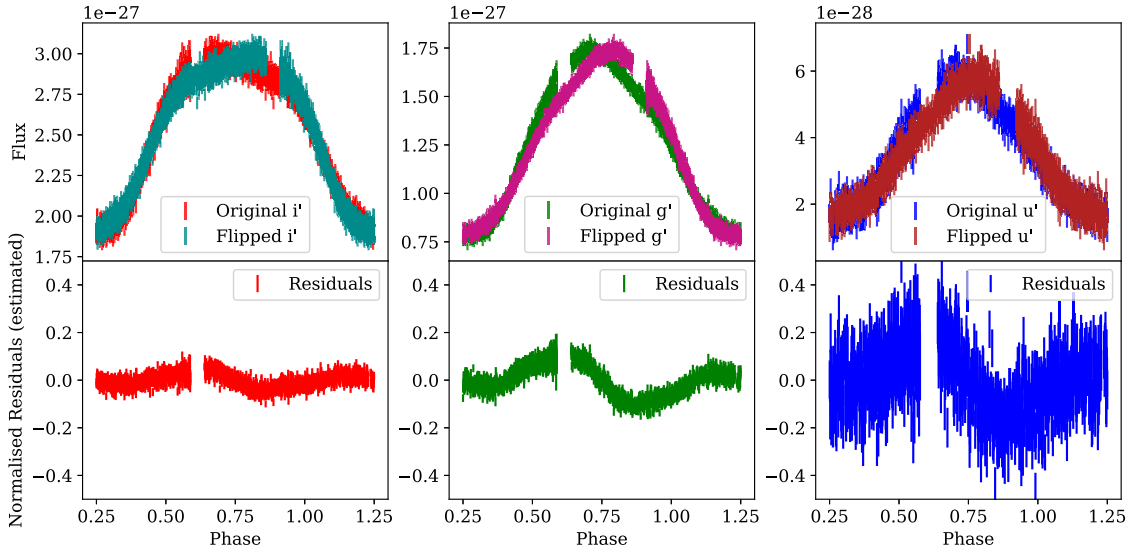

Figure 4. As Fig. 3, for J1227. The light curves were trimmed to remove the region of large scatter around phase 0.6 to. Note that the shape now reflects that of a second-harmonic sinusoid compared to the fundamental sinusoid seen in J1023.

temperature of the companion, $T_{\rm irr}$; the distance modulus, DM; the companion's projected radial velocity amplitude, K_2; the mass ratio (defined as the ratio of the pulsar mass to the companion mass), q; the co-rotation coefficient, Ω; the gravity darkening coefficient, $\beta_{\rm g}$; and the V-band extinction coefficient, A_v. Note that while the ICARUS code uses the DM as a model parameter, in this work we discuss the distance which is derived from this.

The filling factor is defined as the ratio of the stellar surface radius in the direction of the pulsar to the distance to the L1 point. We also derive a volume-average filling factor, which is a representation of the volume of the star to the volume of the RL, $f_{\rm VA} = \langle R \rangle / \langle R_{\rm RL} \rangle$. We fix the co-rotation coefficient to $\Omega = 1$, as we assume both systems are tidally locked, and for both sources we fix $\beta_{\rm g} = 0.08$ as we assume the late-type companion stars have large convective envelopes (Lucy 1967). As well as the volume-averaged filling factor and distance, we also derive the pulsar mass, $M_{\rm psr}$ and the blackbody-equivalent temperatures of the day and night side of the companion.

Relations connecting some of the parameters previously introduced and the orbital ephemerides are also considered in our modelling. In particular, the mass ratio follows the relation

$$q = \frac{K_2 P_B}{2\pi a_1}, \tag{1}$$

where P_B is the orbital period and a_1 is the projected semimajor axis of the pulsar, derived from radio timing (Roy et al. 2015 and Archibald et al. 2009 for J1227 and J1023, respectively).

Finally, we allow the systemic velocity, Γ_v, to be a free parameter as our radial velocity data are not mean-subtracted. At each step in the MCMC chain, we use the ICARUS code to determine the effective centre-of-light radial velocity, $v_{\rm eff}$, of the companion, evaluated using

a model atmosphere corresponding to the wavelength range of the spectroscopic radial velocity curve. In this case, this corresponds to the SDSS *r'*-band. The amplitude of this effective radial velocity curve is defined as $K_{\rm eff}$. We then fit for and subtract any linear offset between the modelled and measured radial velocity curves, and calculate the residuals. These residuals are combined with the residuals from the modelled light curve to calculate the posterior probability at each step in the chain.

To determine the model parameters, we used the MULTINESTed sampler, MULTINEST (Feroz, Hobson & Bridges 2009), implemented in Python as PYMULTINEST (Buchner et al. 2014). This method also allows us to directly compare the Bayesian evidence of each choice of model. In this paper, this is quoted as the natural logarithm of the model evidence, $\log Z$, and the reduced χ^2 is determined from the best posterior solution (as opposed to the best likelihood solution).

The selection of priors is very important as the model is extremely degenerate; where possible, we use priors on parameters informed by published measurements. For these we use Gaussian priors, centred on the literature value with standard deviation equal to the given uncertainties (i.e. the 68 per cent significance). For parameters with no known constraints, we either use top-hat priors over a range of physically sensible values (such as constraining the temperature to the range of the atmosphere grids) or leave the parameter unconstrained.

4.2 Standard symmetrical direct heating model

Initially, we used a symmetrical direct heating model to act as a benchmark. This model assumes a constant base temperature, T_0, across the companion, then models the effect of heating by assuming that the additional flux is thermalized and locally re-emitted such that we can express the day side temperature, $T_{\rm day}$ as

$$T_{\rm day}^4 = T_0^4 + T_{\rm irr}^4, \tag{2}$$

where $T_{\rm irr}$ is the so-called irradiation temperature. The effect of gravity darkening is applied prior to the irradiation to give the temperature distribution of the companion. Irradiation effects take into account the distance between the companion and the pulsar and the incidence angle of the irradiation.

For J1227 the free parameters in this initial model were the $\cos i$, T_0, and $T_{\rm irr}$, *DM*, K_2, and *f*. While de Martino et al. (2014) suggest an inclination of $43^\circ < i < 73^\circ$ and the modelling of de Martino et al. (2015) constrains $46^\circ < i < 65^\circ$, we opted to leave the inclination unconstrained to perform independent modelling (i.e. not biased by previous studies).

We used top-hat priors on the temperatures, setting the limits in accordance with the range of temperatures covered by our model atmosphere grids: 1300–10 000 K. We left the filling factor mostly unconstrained, with limits $0.0 < f < 1.0$, as we expect the RL to be mostly full, but have no physically imposed minimum filling factor.

The priors on the DM were calculated following the method described in Luri et al. (2018), using the joint probability distribution of distances derived from the *GAIA* parallax measurement combined with the model of Galactic MSP densities from Levin et al. (2013). The *GAIA* parallax was significant, at 0.623 ± 0.168 mas, and so this dominated the distribution.

We constrain the companion velocity, K_2, based on the radial velocity amplitude inferred from spectroscopy by de Martino et al. (2014); $K_2 = 261 \pm 5$ km s^{-1}. Note that the radial velocity data are not publicly available at the time of writing. Rather than using a simple Gaussian prior on this value, we instead use the radial velocity curve method described in the previous section. Our radial velocity

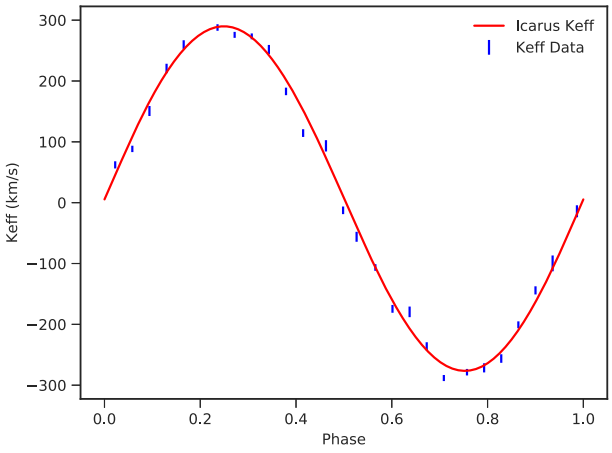

Figure 5. Radial velocity fitting curve for J1023. The points in blue are the radial velocity measurements from spectroscopy (Shahbaz et al. 2019), and in red is the best-fitting radial velocity curve from ICARUS. The red RV curve is calculated at each step in the MULTINEST sampler and the χ^2 value from the fit to the data is added to the posterior distribution. $K_{\rm eff}$ is the effective centre-of-light radial velocity of the companion.

'curve' consists of this single value at phase $\phi = 0.25$, the pulsar inferior conjunction, where the maximum projected velocity occurs. This method ensures the radial velocity amplitude from spectroscopy is corrected to the centre of mass of the companion.

We also use Gaussian priors on the derived parameter $V\sin(i) = 86 \pm 20$ km s^{-1}, the companion rotational velocity, obtained from the same spectroscopy, using the relation derived in Wade & Horne (1988),

$$V \sin(i) = (K_1 + K_2) R_2(f), \tag{3}$$

where K_1 is the radial velocity of the pulsar, and $R_2(f)$ is the volume-averaged radius of the companion star (in units of *a*) evaluated at a given RL filling factor, *f*. We therefore use this to constrain both the filling factor and companion system velocity. We obtain K_1 from radio timing (Roy et al. 2015), while K_2 and $R_2(f)$ will be calculated by the ICARUS model.

For J1023, we used the same top-hat priors on T_0, $T_{\rm irr}$, and *f* as with J1227. While a well-constrained inclination can be derived from the results of Deller et al. (2012), $42 \pm 2^\circ$, these calculations assume that the companion is RL filling (Thorstensen & Armstrong 2005). As such, we do not use any priors on the inclination.

Deller et al. (2012) accurately determined the distance to the system from parallax measurements using long baseline radio interferometry to be $d = 1.368^{+0.042}_{-0.039}$ kpc. This is much more precise, with a lower uncertainty than estimating the distance using the *GAIA* parallax method, and so this was used to inform our DM priors.

For K_2, there are radial velocity measurements available from Shahbaz et al. (2019); however, the heating of the companion distorts the radial velocity curve. This results in variable measurements of the radial velocity semi-amplitude. We take the measurements obtained from 2009 ISIS observations in the pulsar state of metallic absorption lines which correspond to a radial velocity semi-amplitude of $K_2 = 276.3 \pm 5.6$ km s^{-1}. Instead of using these to inform a Gaussian prior on K_2, we use the data presented in their work to fit a radial velocity curve using the method described in Section 4.1. Fig. 5 shows these data and the fitted radial velocity curve. From the same work we used the $V\sin(i)$ measurement of $V\sin(i) = 77.7 \pm 2.7$ km s^{-1} to constrain *f* and K_2, also from the 2009 ISIS observations of metallic absorption lines.

We also fit the *V*-band interstellar extinction separately for each source. For J1227 we use the prior value $A_V = 0.341$, calculated using the relationship $A_V = 3.1E(B-V)$ (Cardelli, Clayton & Mathis 1989) from the colour excess presented in de Martino et al. (2014), in turn calculated from the N_H column density presented in de Martino et al. (2010). We allow for a 20 per cent uncertainty on this value. For J1023 we test two methods. First, we used the colour excess determined in Shahbaz et al. (2015; again using the N_H column density) to calculate the extinction and the same relationship, obtaining $A_V = 0.2263$ and allowing for the same 20 per cent uncertainty. Secondly, we use the Pan-STARRS dust maps of Green et al. (2018) to obtain $A_V = 0.109$ As these methods do not produce consistent extinction coefficients, we compared the evidence of models with each A_V prior and otherwise identical parameters. For both sources, we use the reddening coefficients of Schlafly & Finkbeiner (2011) to calculate the appropriate extinction for each band.

4.3 Single-spot heating model

We extended the symmetrical model to include a single hotspot on the companion's surface. This was motivated by the successful modelling of similar asymmetries in other redback sources using a single-spot model (e.g. Romani & Sanchez 2016; Shahbaz, Linares & Breton 2017; Nieder et al. 2020; Clark et al. 2021). Our motivation for the inclusion of a hotspot is largely empirical; however, we discuss two possible physical origins of the asymmetric heating in Section 3: heating from X-rays reprocessed by a swept-back shock and thermal winds on the companion surface.

Each spot introduces four free parameters: the spot temperature, $T_{\rm spot}$, the spot radius, $R_{\rm spot}$, and the spot position angles, θ_s, ϕ_s. A full description of the spot geometry and heating contribution is presented in Clark et al. (2021), and a summary of the model extensions used in this work is included in appendix A. We use a single spot as using more than one is likely to overfit the data while also being more computationally expensive and significantly increasing the degeneracy of the parameter space. The priors on the spot temperature and radius are uniform over the ranges $0\,{\rm K} < T_{\rm spot} < 10\,000$ K and $0^\circ < R_{\rm spot} < 90^\circ$, respectively. This upper bound on the spot temperature also corresponds with the maximum temperature covered by the atmosphere grids used.

We note that the asymmetric heating caused by a hotspot on the leading edge of the companion (the side of the companion moving 'forwards' through the orbit) can also be described by a 'cold' spot on the trailing edge (the side moving 'backwards'). As such, we also performed fitting with a cold spot with a negative spot temperature, $T_{\rm spot} < 0$. We use uniform priors on $\cos\theta_s$ and uniform priors on the ϕ_s angle. To constrain the spot temperature and radius, we use Gaussian priors on the intensity of the flux from the spot, $I \propto T^4R^2$, with a mean of $I = 0$ and a width of $\sigma_I = 10^{12}$. This was chosen in order to avoid a very small ($R_{\rm spot} \leq 5^\circ$), very hotspot, since this prior favours cooler larger spots.

4.4 Heat redistribution

As detailed in Section 5, our modelling with both the symmetric and hotspot models produced results that were not reliable, and indeed indicated that neither model sufficiently describes the highly asymmetric light curves of these systems. As a result, we additionally used a further extension of the ICARUS code which directly models heat redistribution via diffusion and convection within the outer envelope of the companion. We implement the treatment in Voisin et al. (2020), though we acknowledge also the treatment of wind circulation in Kandel & Romani (2020) as a specific case of the latter. We continue our use of MULTINEST evidence sampling to constrain the model parameters and heat redistribution laws. While the direct heating model assumed a constant companion base temperature (save for the effects of gravity darkening) and the hotspot extension assumes an additional fixed temperature source, the heat redistribution model allows for parallel (that is, with no radial component) energy transport within the outer shell. The details of this model are presented in appendices A and B, while a full treatment can be found in Voisin et al. (2020).

This model allows for a choice of convection profile, $f(\theta)$. We initially chose a linear profile, $f(\theta) = v$, where v is the strength of the convection current in energy flux per unit temperature and is the first additional model parameter. This profile describes constant longitudinal advection. We allow for the diffusion coefficient, defined in appendix A, to depend on the local temperature following a power law of index, Γ. We performed fits with both $\Gamma = 0$ for linear diffusion and with the diffusion index as a free parameter. The diffusion coefficient, κ, is the last additional model parameter. When $\kappa = 0$, the diffusion is switched off and the model becomes convection only. In this case, this model is equivalent to that in Kandel & Romani (2020) when used with a 'bizone' convection profile. However, we do not use that profile in this work. We performed fits with both $\kappa = 0$ and κ as a free parameter.

5 RESULTS

5.1 J1227

5.1.1 Standard model

As expected, this model was unable to account for the asymmetries in the light curves, reflected by a reduced chi-squared value of $\chi^2_\nu = 2.37$ for our best-fitting model and evidence of -5177.6. We note that the evidence provides little information on its own, but is included as a means to compare each model. As a result, the model is a poor fit, and the best-fitting parameters are likely erroneous; for example, the sampler favours a nearly edge-on inclination of $i = 88.3^{+0.7^\circ}_{-1.0}$, converging at the upper limit of the prior. An inclination this close to 90° is highly unlikely as X-ray eclipses have not been observed (de Martino et al. 2014). In light of this, we include an additional constraint in subsequent fits: the pulsar (and hence the inner region of the accretion disc) must not be eclipsed by the companion star at any orbital phase. This results in an upper limit on the inclination around $i_{\rm max} \sim 77^\circ$, though the exact value depends on the filling factor and mass ratio parameters.

The companion velocity is derived from the inclination and K_2 (and therefore $K_{\rm eff}$) in our model such that the fit with velocity $K_{\rm eff} = 269^{+5}_{-5}$ km s^{-1}, consistent with the de Martino et al. (2015) velocity, corresponds to an unrealistically low-pulsar mass of $M_{\rm psr} \sim 0.9$ M$_\odot$. Loosening our prior on K_2 results in a more acceptable pulsar mass of $M_{\rm psr} \sim 1.2$ M$_\odot$ but a companion radial velocity of $K_{\rm eff} = 308^{+12}_{-20}$ km s^{-1}, which is clearly not consistent with the literature. The companion temperature ($T = 5452^{+19}_{-20}$ K) and irradiation temperature ($T_{\rm irr} = 5230^{+26}_{-28}$ K) do agree with those determined in de Martino et al. (2015), as these parameters are primarily influenced by the colour information rather than the shape of the light curves. However, we do not reproduce their filled RL ($f = 1.0$); instead we determine $f = 0.825^{+0.002}_{-0.002}$, corresponding to a volume-average filling factor of $f_{\rm VA} = 0.95$. Note also that their modelling uses a symmetric model. Considering these discrepancies in addition to a poor overall fit, we conclude

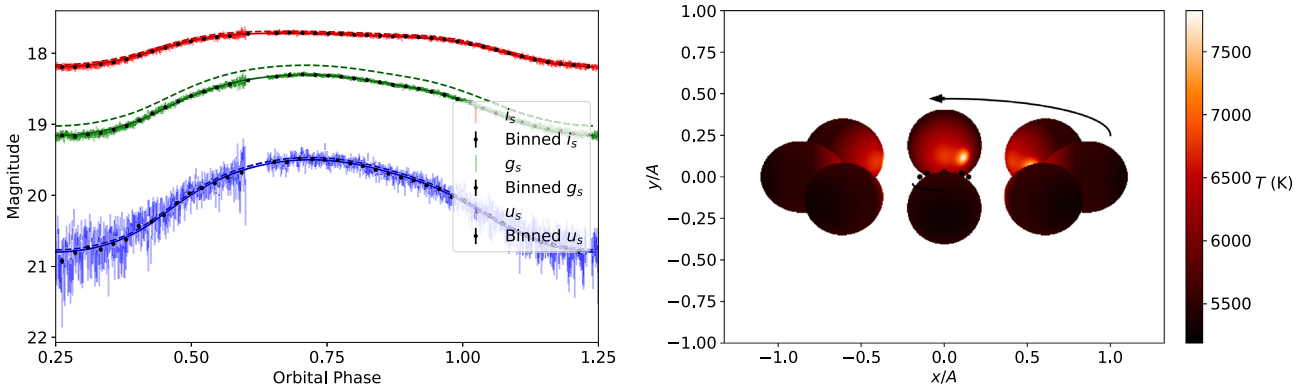

Figure 6. Left: i_s, g_s, and u_s light curves of J1227 overlaid with the best-fitting hotspot model. The dashed lines show the model light curve without band calibration corrections. Right: temperature distribution of companion – note how the inclination is such that the companion only just avoids eclipsing the pulsar at inferior conjunction.

that the standard ICARUS heating model is not appropriate for this source.

5.1.2 Hot spot model

The hotspot heating model was able to account for the majority of the asymmetry with $\chi^2_\nu = 1.11$ and evidence of -3345.1, indicating a significantly improved fit over the symmetric model. The best-fitting hotspot model is shown in Fig. 6. We find that the filling factor determined by our best-fitting model, $f = 0.838 \pm 0.003$ ($f_{\rm VA} = 0.958 \pm 0.003$), also indicates that the companion is not RL filling and is consistent with the symmetric model result. The system distance, $1.82^{+0.09}_{-0.09}$ kpc, and best-fitting temperatures, $T_0 = 5556^{+14}_{-15}$ K and $T_{\rm irr} = 5312^{+21}_{-21}$ K, are also broadly similar to the symmetric model.

As with the direct heating model, the model prefers a $K_{\rm eff}$ comparable to that obtained from the spectroscopy, while the pulsar mass is unreasonably low at $0.93 \pm 0.04\,{\rm M}_\odot$. We therefore constrained the pulsar mass to the range $1.0\,{\rm M}_\odot < M_{\rm psr} < 3.0\,{\rm M}_\odot$ for a repeat of this fit. However, the companion effective radial velocity with this constraint, 307^{+10}_{-10} km s^{-1}, is unacceptably large compared to the spectroscopic measurement of de Martino et al. (2014). This occurs as K_2 increases to compensate for the high inclination, increasing q as well.

The inclination again indicates a nearly edge-on system with a best-fitting value of $76.6^{+0.6\circ}_{-1.2}$. The shape of the posterior distribution is skewed, showing that the model has converged with an inclination very close to the limit imposed by the eclipse limit. This is illustrated in the corner plot in Fig. 7. While the hotspot model provides an improved fit to the data, the best-fitting values of the inclination, pulsar mass, and companion radial velocity are not suitable.

5.1.3 Cold spots

The asymmetry of the light curve of J1227 is stronger in the cooler i_s and g_s-bands than the u_s-band, suggesting that a cold spot may be better suited to model the asymmetry. We repeated the analysis in presented Section 5.1.6 using a cold spot model and found that the same trends were present. However, the distances and masses are larger than with the hotspot and for all inclinations the fitting is poorer. Notably, the effective $K_{\rm eff}$ velocities are consistently more than 1σ larger than the spectroscopic K_2, whereas these velocities were consistent when using the hotspot. Comparing the evidence for the $i = 60^\circ$ run as an example, this was -3933.7 for the cold spot compared to -3600.8 for the hotspot, indicating a less favourable model. These factors indicate that the hotspot model is preferred over the cold spot for J1227.

5.1.4 Heat redistribution

We performed several fits using the heat redistribution model introduced in Section 4.4, though none improved on the model parameters or evidence of the best-fitting hotspot model; that is, the edge-on inclination and small pulsar mass were still favoured. These results are presented in Table 2 alongside the results from the symmetric and single spot models. Note the similarity between the parameters of the two models, which results in indistinguishable model light curves. While the diffusion coefficient (κ) must be positive, we used a lower bound of -100 to avoid boundary effects around 0. As such, the negative value of diffusion coefficient in model HR1 (linear diffusion and convection) is unphysical and suggests a true value of 0. Additionally, the uncertainty of this value is likely underestimated as the posterior distribution converged on the boundary. Indeed, the model parameters of HR1 and HR2 are otherwise consistent within uncertainties, suggesting that the model with convection only is a better description of the system. However, the model evidence and χ^2 in both cases favours the hotspot model.

5.1.5 Modelling assuming a filled Roche Lobe

We also performed fits where the RL is filled with $f = 1.0$ as in de Martino et al. (2014). Under this assumption, the symmetric model provided an unsatisfactory fit similar to the f-free symmetric model and so was discarded. Modelling with a hotspot returned an acceptable fit with evidence of –3871.8 and a reduced χ^2 of 1.32, comparable but not better than the f-free case. However, the best-fitting value of K_2 corresponds to a velocity of $K_{\rm eff} = 217 \pm 5$ km s^{-1}, which is more than eight standard deviations from the spectroscopic measurement.

5.1.6 Modelling with fixed inclination

With the inclination otherwise unconstrained, both the standard and hotspot models strongly favour an edge-on system with an inclination close to 90°. A system this edge-on is ruled out by the non-detection of X-ray eclipses, suggesting an inclination of $i \lesssim 73^\circ$ (de Martino et al. 2014), and the lack of eclipses seen in spectra. Furthermore,

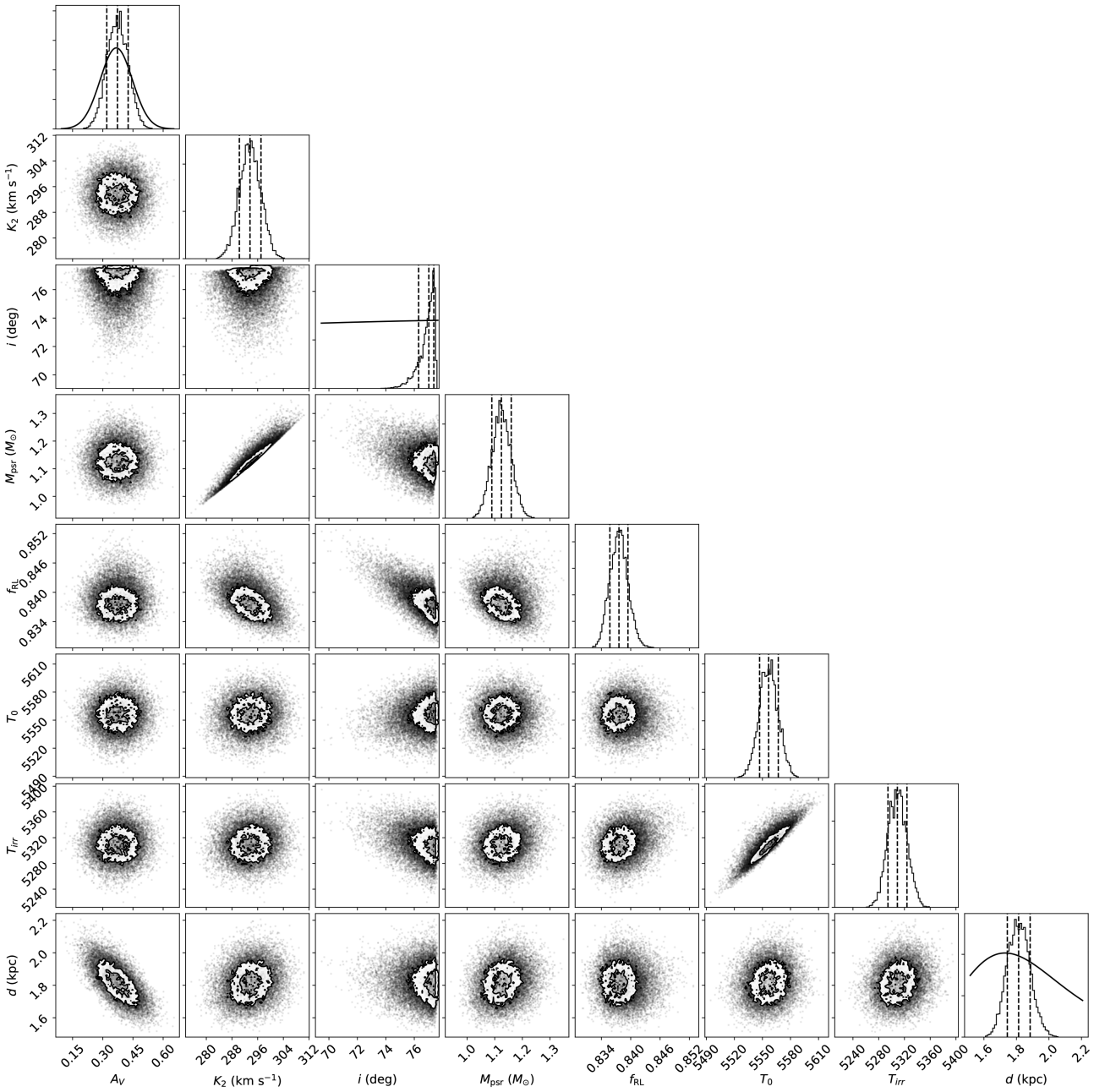

Figure 7. Corner plot of selected parameters of the J1227 hotspot model. Not shown are the hotspot parameters and the mass ratio. The plots along the diagonal are the posterior distributions of the parameters; the solid black lines on these are the prior distributions. The remaining plots show the position of walkers, illustrating covariance between parameters. Note the posterior distribution of the inclination, with the walkers converged against the upper limit set by the zero eclipse width.

when the radial velocity constraint from de Martino et al. (2014) is enforced the model returns a pulsar mass in the range $M_{\rm psr} \sim 0.8-1.0{\rm M}_\odot$, which is clearly inappropriate. Conversely, relaxing this constraint we obtain a reasonable pulsar mass of $M_{\rm psr} \sim 1.4{\rm M}_\odot$ but a value for K_2 which is too large, i.e. ∼330 km s^{-1}.

To attempt to overcome these discrepancies, we performed modelling of the system with the inclination fixed at each of $i = 40^\circ$, 50°, 60°, and 70°, using the hotspot model. Broadly, we observe that the pulsar mass, T_0, and filling factor are negatively correlated with inclination, while the system distance and irradiation temperature are positively correlated. The other parameters are not affected within uncertainties. We summarize these results in Table 3, though we do not cover the full results of the fit with $i = 40^\circ$ as the pulsar mass of $M_{\rm psr} \geq 3.0{\rm M}_\odot$ and the distance of $d = 2.41 \pm 0.12$ kpc are both unreasonably large, suggesting that inclinations this low can be safely discarded.

It is worth noting that while the fit value of K_2 does not seem to be correlated with the inclination, the effective value appears to have a slight positive correlation with the inclination. However, the $K_{\rm eff}$ is consistent with the de Martino et al. (2014) radial velocity for inclinations 50°, 60°, and 70°, suggesting that the prior on the radial velocity is still tightly constraining. Likewise, the RL is consistently underfilled at all inclinations. We note that the evidence of each fit is also correlated with the inclination in a direction that

Table 2. Numerical results for the modelling of J1227, including from top to bottom the model parameters: selected derived parameters, and model statistics. From left to right: standard symmetric model, single hotspot model, heat redistribution with linear diffusion and constant advection profile (HR1), and heat redistribution with convection only (HR2). $\log Z$ is the natural logarithm of the model evidence and χ^2_ν is the reduced chi squared value with $\nu = 5908$ data points. Note that the inclination of the symmetrical model is higher than the others as the constraint described in Section 5.1.1 is not applied.

Parameters	Symmetrical	Single spot	HR 1	HR2
Inclination, i (°)	$88.3^{+1.3}_{-2.0}$	$76.6^{+0.6}_{-1.2}$	$77.1^{+0.1}_{-0.15}$	$77.0^{+0.2}_{-0.3}$
Mass ratio, q	$5.6^{+0.1}_{-0.1}$	$5.8^{+0.1}_{-0.1}$	$5.48^{+0.07}_{-0.07}$	$5.5^{+0.1}_{-0.1}$
Radial velocity, K_2 (km s^{-1})	282^{+5}_{-5}	294^{+4}_{-5}	277^{+3}_{-4}	277^{+5}_{-5}
Filling factor, f	$0.825^{+0.002}_{-0.002}$	$0.838^{+0.003}_{-0.003}$	$0.850^{+0.002}_{-0.002}$	$0.852^{+0.002}_{-0.002}$
Base temp., T_0 (K)	5452^{+19}_{-20}	5556^{+14}_{-15}	5584^{+11}_{-11}	5585^{+15}_{-15}
Irradiation temp., $T_{\rm irr}$ (K)	5230^{+26}_{-28}	5312^{+21}_{-21}	5479^{+16}_{-15}	5489^{+22}_{-21}
Spot temp., τ (K)	–	2100^{+200}_{-200}	–	–
Spot radius, ρ (°)	–	$7.8^{+0.6}_{-0.5}$	–	–
Spot polar angle, θ (°)	–	95^{+2}_{-2}	–	–
Spot azimuth angle, ϕ (°)	–	-27^{+1}_{-1}	–	–
Diffusion coeff., κ (W K^{-1} m^{-2})	–	–	-95^{+7}_{-3}	0
Diffusion index, Γ	–	–	0	–
Convection amp., v (J m^{-2} K^{-1})	–	–	3230^{+43}_{-45}	3260^{+22}_{-21}
Volume-averaged f, $f_{\rm VA}$	$0.952^{+0.001}_{-0.001}$	$0.959^{+0.001}_{-0.001}$	$0.965^{+0.002}_{-0.002}$	$0.966^{+0.001}_{-0.001}$
Effective radial velocity, $K_{\rm eff}$ (km s^{-1})	269^{+5}_{-5}	277^{+4}_{-5}	263^{+3}_{-3}	263^{+5}_{-5}
Distance, d (kpc)	$1.64^{+0.09}_{-0.09}$	$1.82^{+0.09}_{-0.09}$	$1.84^{+0.06}_{-0.06}$	$1.79^{+0.1}_{-0.1}$
Pulsar mass, $M_{\rm psr}$ ($M_\odot$)	$0.93^{+0.04}_{-0.04}$	$1.13^{+0.05}_{-0.04}$	$0.96^{+0.03}_{-0.03}$	$0.96^{+0.05}_{-0.04}$
Blackbody day temp. (K)	6040	6170	6200	6210
Blackbody night temp. (K)	5310	5410	5430	5430
Reduced chi-squared, χ^2_ν	2.37	1.11	1.38	1.38
Model evidence, $\log Z$	−5177.6	−3345.1	−3906.4	−3906.0

Table 3. Model parameters and MULTINEST evidence for fixed-inclination modelling of J1227 at $i = 50°, 60°, 70°$. This model has $\nu = 5908$ data points.

Model Parameters	$i = 50°$	$i = 60°$	$i = 70°$
f	$0.901^{+0.02}_{-0.02}$	$0.866^{+0.002}_{-0.002}$	$0.841^{+0.002}_{-0.002}$
$M_{\rm psr}$ ($M_\odot$)	$2.1^{+0.1}_{-0.1}$	$1.41^{+0.06}_{-0.06}$	$1.09^{+0.05}_{-0.05}$
d (kpc)	$2.1^{+0.1}_{-0.1}$	$1.8^{+0.1}_{-0.1}$	$1.67^{+0.09}_{-0.09}$
T_0 (K)	5233^{+16}_{-16}	5288^{+15}_{-17}	5329^{+17}_{-19}
$T_{\rm irr}$ (K)	5356^{+26}_{-26}	5184^{+23}_{-26}	5080^{+26}_{-28}
K_2 (km s^{-1})	282^{+5}_{-5}	280^{+5}_{-5}	280^{+5}_{-5}
$K_{\rm eff}$ (km s^{-1})	258^{+5}_{-5}	262^{+5}_{-5}	264^{+5}_{-5}
χ^2_ν	1.43	1.30	1.24
$\log Z$	−4099.9	−3837.3	−3690.3

suggests the model favours a more edge-on system, echoing what we observed when modelling with the inclination unconstrained: an edge-on inclination is favoured despite strong penalties from priors. We attempted modelling with the inclination tightly constrained rather than fixed at $60 \pm 1°$; however, the inclination did not converge to a solution after ∼5 times the usual computing time, suggesting this configuration is not appropriate. While this investigation shows the behaviour of the model at more face-on inclinations, the reason that the unconstrained inclination consistently converges to $i \sim 90°$ is still unclear.

We constructed a mass–mass plot using the results in Table 3, shown in Fig. 8. This plot reveals constraints that we can apply to the masses of the companion and pulsar. We calculate a lower limit to the mass ratio, $q_{\rm min}$, from the centre-of-light $K_{\rm eff}$ radial velocity. Since in ICARUS, the mass ratio is calculated from the larger centre-of-mass K_2, this $q_{\rm min}$ acts as a lower bound to the pulsar mass at each inclination. These K_2 velocities at each inclination therefore correspond to the best-fitting mass ratio, and are consistent across the whole range to within the uncertainties. To further constrain the object masses, we interpolated the model distance estimates at each inclination in the allowed region of the plot. Then, by using the same prior distribution used during the fitting (a combination of *GAIA* parallax, galactic MSP density, and velocity distributions and the DM distance), we calculated the confidence interval over the mass–mass plane. This shaded region indicates that the more edge-on inclinations produce more favourable distances. Indeed, these also correspond to better χ^2_ν values and evidence. Using the evidence alone, the most favoured inclination is $i = 70°$; however, this is a comparatively worse evidence than the best-fitting free inclination model. However, we can conclude that for the range of inclinations $i \sim 50°$–$70°$, we obtain a pulsar mass in the range $M_p \sim 1.09$–$2.0\ M_\odot$ and a companion mass in the range $M_c \sim 0.2$–$0.37\ M_\odot$. The lower bound pulsar mass of $M_{\rm psr} \approx 1.09\ M_\odot$ at $i = 70°$ would make J1227 the least massive known MSP and indeed very close to the lowest possible pulsar mass under current formation mechanisms.

Since the mass estimates at more face-on inclinations more closely resemble those found in spiders; this is at odds with the better evidence and distance estimate at 70°. Considering these discrepancies, we may surmise that the hotspot model is not a complete description of the system.

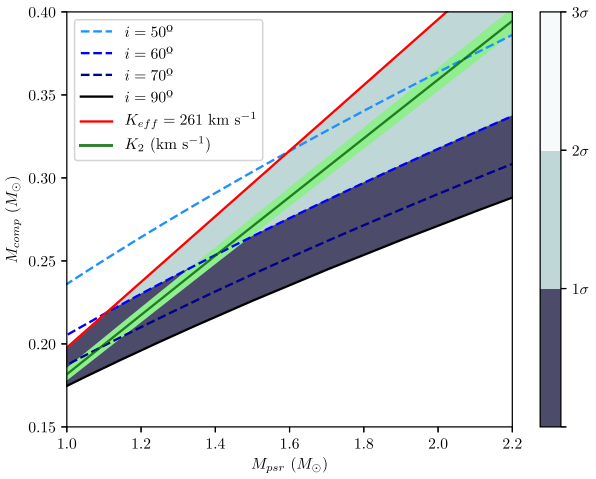

Figure 8. The mass ratio calculated from the centre-of-light $K_{\rm eff}$ value, in red, provides us with a lower limit of the pulsar mass for each inclination, while the best-fitting mass ratio from each fit's K_2 is in green. The binary mass function at each inclination is shown by the series of blue dashed lines, with the absolute limit at $i = 90^\circ$ shown by a solid black line. As such, the excluded region of the mass–mass plot is in white. The best-fitting model distance at each inclination is interpolated over the mass–mass plane. The shaded area then represents the corresponding confidence interval of the distances with respect to the distance prior.

5.2 J1023

5.2.1 Standard model

As with J1227, the symmetric heating model did not provide a good fit to the data, with best-fitting reduced χ^2 value of $\chi^2_\nu = 6.20$ ($\nu = 3821$) and evidence of -5295.0. This is a comparatively worse fit than the same modelling of J1227, in part because smaller error bars from a brighter source and better observing conditions make the asymmetry more significant compared to the noise, with the u_s-band fit especially poorly. The best-fitting parameters are summarized in Table 4.

We determine an inclination angle of $i = 46.4^{+0.5^\circ}_{-0.7}$, which is consistent with the range of possible inclinations of Archibald et al. (2009), $34^\circ < i < 53^\circ$, and consistent with the inference in Thorstensen & Armstrong (2005) that $i < 55^\circ$. Note that these literature values were calculated under the assumption that the companion is RL-filling. We again obtain an RL filling factor of significantly less than 1.0, though there is a strong negative correlation with the inclination such that at an inclination consistent with the Archibald et al. (2009) calculation, the filling factor approaches $f = 1.0$.

The system temperatures indicate that the companion is not as strongly irradiated as in J1227. A best-fitting distance of $d = 1.26^{+0.02}_{-0.01}$ kpc broadly agrees with the radio parallax measurement of $1.368^{+0.042}_{-0.039}$ kpc from Deller et al. (2012). Note that across all models the distance is consistently underestimated; this is discussed in Section 6.4. This fit produces a radial velocity of $K_{\rm eff} = 287 \pm 3$ km s^{-1}, corresponding to a mass ratio of $q = 7.8 \pm 0.05$ which is comparable but not consistent with the result from radio timing in Archibald et al. (2009). This is as expected, as the radial velocity parameter appears to be consistent with the upper bound of measurements from the spectral lines in Shahbaz et al. (2019), and the mass ratio is calculated directly from this velocity. Unlike with our modelling of J1227, the posterior distributions of these model parameters, notably the mass, generally converged within the range of expected literature values. However, the large χ^2 value leads us to again conclude that the symmetric model is insufficient.

5.2.2 Hot spot model

With $\chi^2_\nu = 1.20$ and a peice of evidence of -2293.9, the hotspot model provides a much better fit to the data than the symmetric model, capturing the asymmetries to a good degree. The parameters of the best-fitting model are shown in Table 4. The filling factor remains below 1.0 and the inclination is again consistent with that inferred from radio timing from Archibald et al. (2009). The distance is also broadly consistent with the interferometry distance in Deller et al. (2012), 1.28 ± 0.02 kpc compared to 1.368^{+42}_{-39} kpc. Considering the best-fitting spot parameters, the spot radius of $48 \pm 2^\circ$ and position near the companion pole is strikingly similar to the spot properties seen in Kandel et al. (2020). The temperature distribution of the companion is shown alongside the best-fitting model in Fig. 9. We expect tMSPs to host massive neutron stars, and the constrained mass of $M_{\rm psr} = 1.89^{+0.10}_{-0.09}$ is no exception. Note, however, that there is a moderate inconsistency between the determined pulsar masses.

5.2.3 Heat redistribution

Choosing a diffusion index of 0 (linear diffusion) and a constant advection polar convection profile, we ran an initial model of the light curve. We found that the asymmetry was well fitted, but with a marginally worse evidence and reduced χ^2 than the best-fitting hotspot model. Since the heat redistribution model also allows for a range of combinations of diffusion and convection, the results of *(1)* a model with convection only, and *(2)* convection with linear diffusion (i.e. with a zero diffusion index) are shown in Table 4. However, model *(3)* with convection and temperature-dependent diffusion converged to a solution with a very large diffusion index which caused significant aliasing in the temperature distribution of the companion; as such these results have not been included. Comparing the other two models, the evidence favours a model with convection and linear diffusion, despite the fact that the best-fitting distance for this model is significantly below the literature value.

6 DISCUSSION

6.1 Filling factor

One consistency across all models is an underfilled RL with our modelling returning values in the range $f \sim 0.825{-}0.90$ for J1227 and $f \sim 0.81{-}0.94$ for J1023. This is at odds with our expectations for these sources: as they are both tMSPs we would expect the RLs to be full or nearly filled in the RP states, given they have transitioned from RL overflow in their AP states. However, when considering the volume-averaged fill factor, the values of $f_{\rm VA} = 0.958$ and 0.994 for the best-fitting models of J1227 and J1023, respectively, tell a story more consistent with our initial expectations: that the RL is indeed mostly full.

Fig. 10 illustrates the relationship between these two parametrizations. When considering the proximity of the companion star to a state of RL overflow, f is a more useful description as it gives the distance of the star surface to the L1 point. However, the volume-averaged filling factor gives a clearer picture of the size of the star relative to its RL – in these cases illustrating that a substantial increase in the volume-averaged radius of the star is not necessarily required for RL overflow to begin. For J1023 in particular, the volume-averaged fill

Table 4. Numerical results for the modelling of J1023, including from top to bottom: the model parameters, selected derived parameters, and model statistics. This model has $\nu = 3821$ data points. From left to right: standard symmetric model, single hotspot model, heat redistribution with linear diffusion and constant advection profile (HR1), and heat redistribution with convection only (HR2). Note the similarity between the blackbody temperatures of each model despite the large range of T_0 and $T_{\rm irr}$ temperatures.

Parameters	Symmetrical	Single spot	HR 1	HR2
Inclination, i (°)	$46.4^{+0.5}_{-0.7}$	$45.1^{+0.8}_{-0.9}$	$48.7^{+0.20}_{-0.23}$	$45.3^{+0.6}_{-0.5}$
Mass ratio, q	$7.8^{+0.05}_{-0.05}$	$7.8^{+0.1}_{-0.1}$	$7.87^{+0.04}_{-0.04}$	$7.89^{+0.05}_{-0.05}$
Radial velocity, K_2 (km s^{-1})	295^{+3}_{-3}	295^{+3}_{-3}	$297.0^{+2.3}_{-2.2}$	$298.0^{+2.5}_{-2.5}$
Filling factor, f	$0.86^{+0.01}_{-0.01}$	$0.94^{+0.02}_{-0.02}$	$0.808^{+0.003}_{-0.003}$	$0.864^{+0.007}_{-0.007}$
Base temp., T_0 (K)	5580^{+14}_{-13}	4885^{+31}_{-30}	4477^{+107}_{-43}	5500^{+10}_{-10}
Irradiation temp., $T_{\rm irr}$ (K)	4903^{+26}_{-23}	4677^{+48}_{-45}	7351^{+60}_{-150}	4867^{+15}_{-15}
Spot temp., τ (K)	–	1134^{+32}_{-32}	–	–
Spot radius, ρ (°)	–	48^{+2}_{-2}	–	–
Spot polar angle, θ (°)	–	$8.2^{+1.0}_{-0.8}$	–	–
Spot azimuth angle, ϕ (°)	–	-57^{+5}_{-5}	–	–
Diffusion coeff., κ (W K^{-1} m^{-2})	–	–	93500^{+4000}_{-8000}	0
Diffusion index, Γ	–	–	0	–
Convection amp., υ (J m^{-2} K^{-1})	–	–	52000^{+2000}_{-4000}	8630^{+60}_{-60}
Volume-averaged f, $f_{\rm VA}$	$0.969^{+0.009}_{-0.008}$	$0.994^{+0.004}_{-0.003}$	$0.942^{+0.002}_{-0.002}$	$0.971^{+0.004}_{-0.004}$
Effective radial velocity, $K_{\rm eff}$ (km s^{-1})	287^{+3}_{-3}	283^{+3}_{-3}	$291.0^{+2.3}_{-2.2}$	$290.0^{+2.5}_{-2.5}$
Distance, d (kpc)	$1.26^{+0.02}_{-0.01}$	$1.28^{+0.02}_{-0.02}$	$1.19^{+0.01}_{-0.01}$	$1.30^{+0.02}_{-0.02}$
Pulsar mass, $M_{\rm psr}$ ($M_\odot$)	$1.76^{+0.06}_{-0.05}$	$1.89^{+0.10}_{-0.09}$	$1.69^{+0.03}_{-0.03}$	$1.62^{+0.06}_{-0.06}$
Blackbody day temp. (K)	5820	5700	5750	5750
Blackbody night temp. (K)	5470	5380	5420	5410
χ^2_ν	6.20	1.20	1.26	1.45
log Z	−5295.0	−2293.9	−2462.6	−2633.5

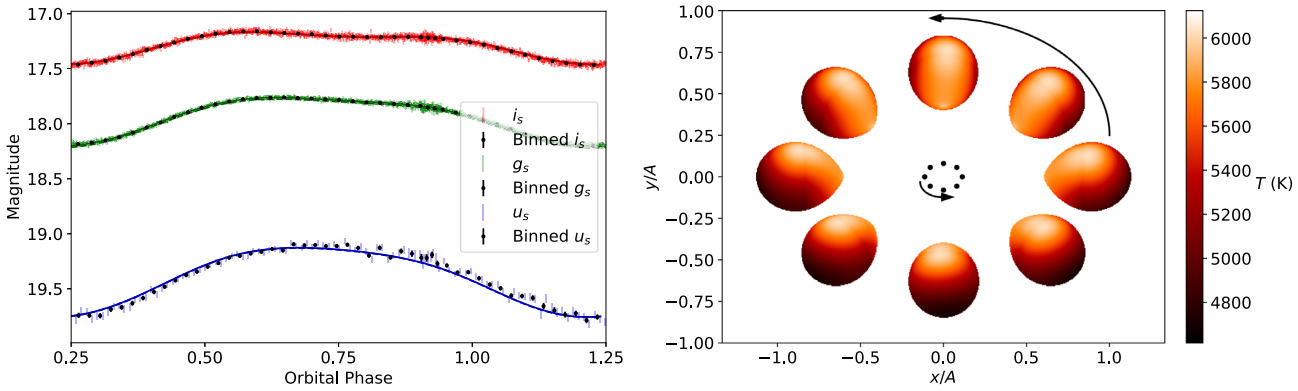

Figure 9. Left: i_s, g_s, and u_s light curves of J1023 overlaid with the best-fitting hotspot model with 40 phase bins in black. Right: temperature distribution of companion, showing the asymmetry which manifests as a large polar spot. The dark band around the star is an artefact due to the plotting only.

factor approaches unity. With a nearly full RL in the RP state, we may consider mechanisms for transitions.

We may assume that if the mass transfer is conservative, then the orbital separation should increase during the AP state in order to conserve angular momentum. This would correspond with an expansion of the companion's RL. While orbital period variations in the RP state have been observed (Archibald et al. 2013), these are over the time-scale of ∼100 d, shorter than the time-scale between transitions of ∼1−10 yr. Furthermore, these variations are not of sufficient magnitude to cause the required changes in RL radius. The observed variation in $T_{\rm asc}$ are of order ∼1 s. With the relation $\Delta T_{\rm asc} \sim \dot{P}_{\rm orb} t_{\rm obs}$, where $t_{\rm obs} \sim 100$ d is the observation time, this corresponds to a change in a of $\Delta a/a \sim 10^{-5}$, a factor of $\sim 10^5$ too small. We assume that a fraction change in a is equivalent to the same fractional change in the RL radius.

Lastly, there appears to be no correlated changes in the orbital period over the several years of data, suggesting the changes are not gradual and continuous as would be the case with steady mass loss from ablation. Instead, a change in the structure of the star without significant mass loss could be explained by the size of the convective envelope decreasing or disappearing completely as the system transitions from the AP to RP state. We assume that the companion stars in redback systems have large convective envelopes, so it is possible that these are 'puffed up' while in the RP state.

The irradiation of the companion by the pulsar wind is known to expand the companion photosphere; however, it is uncertain if this

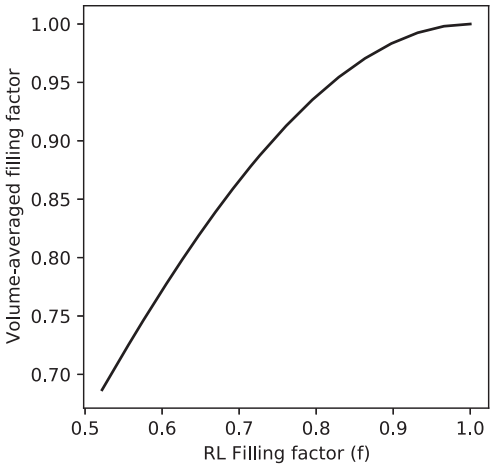

Figure 10. Relationship between filling factor, f, and the volume-averaged filling factor. At lower values of f ($f < 0.6$), the relationship is linear. Considering filling factors for $f > 0.8$, it can be seen how an apparently underfull RL can have a volume-averaged filling factor much closer to unity due to the tidally distorted shape of the companion.

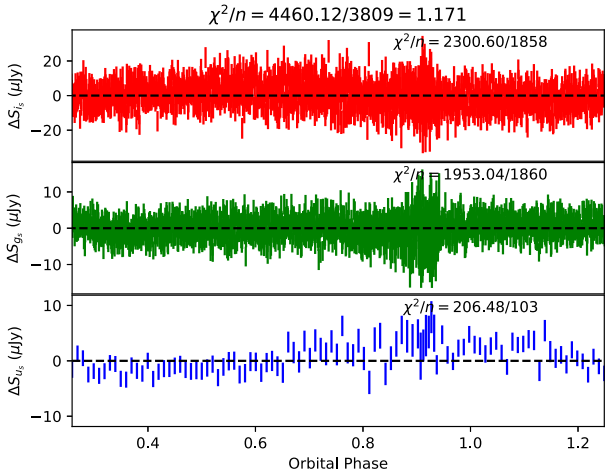

Figure 11. Residuals per band for the best-fitting hotspot model of J1023; note that the y-axis is in units of flux. The u' residuals show a clear systematic pattern that mirrors the sinusoidal shape of the asymmetry in Fig. 3. Note also that the reduced χ^2 value for the u' is significantly larger than that for the other two channels; 1.88 compared to 1.05 for g' and 1.31 for i'.

could occur sufficiently within the transition time-scale. Similarly, if an accretion disc shields the secondary from the pulsar irradiation, it could allow the companion photosphere to gradually contract during the AP state. Consider the Kelvin–Helmholtz mechanism,

$$\tau_{\rm KH} \sim \frac{GM^2}{2RL} \sim \frac{2G\rho M}{3\sigma_{\rm SB}T^4}, \tag{4}$$

where G is the gravitational constant, M is the mass of the star, R is its radius, L is its luminosity, ρ is the mean density of the star, T is its temperature, and $\sigma_{\rm SB}$ is the Stefan–Boltzmann constant (Kippenhahn, Weigert & Weiss 2012). Assuming a mean stellar density of 1 g cm^{-3}, a companion mass of 0.4 M$_\odot$, and a temperature of 5500 K, we obtain a time-scale of $\tau_{\rm KH} \sim 2 \times 10^7$ yr. This is significantly longer than the $\sim$ yr time-scales between tMSP transitions. If we consider the contraction of only the outer convective layer, some fraction k_R of the stellar radius, it is possible a thin layer of the companion could contract and expand within transition time-scales. However, this is highly dependent on the depth of this necessarily thin layer.

In light of this, we consider the discussion of the envelopes of asymptotic giant branch stars in Soker (2015). Following equation (2) in Soker (2015), we separate the companion star into a core of mass $M_{\rm core} = f_c M_c$ and envelope $M_{\rm env} = (1 - f_c)M_c$, where f_c is a fraction between 0 and 1. Assuming the radius of the star is equal to the RL radius, calculated using the Eggleton approximation (Eggleton 1983) with $q = 7.8$, we calculate the Kelvin–Helmholtz time-scale for this envelope to be $\tau_{\rm KH} \sim f_c(1 - f_c) \times 100$ kyr. To obtain a time-scale of order $\sim$10 yr, as expected from the tMSP transition time-scale, we arrive at a mass fraction of $f_c \sim 10^{-4}$. This is a plausible result, suggesting that a fraction of the envelope can be expected to contract within tMSP transition time-scales.

Considering the corner plot in Fig. 7, showing the J1227 hotspot model parameters, strong covariance between the filling factor and inclination can be seen. This covariance indicates a negative correlation such that for a lower (more face-on) inclination, the filling factor would increase towards unity. Given that we suspect the inclination of J1227 to be overestimated in our model, this may suggest that the star may be even closer to filling its RL than inferred. A similar relationship between the distance and filling factor is seen for J1023, where a distance closer to the interferometry measurement results in a filling factor closer to unity.

6.2 Asymmetries

For both sources the hotspot model clearly provides a better fit than the symmetric model – both in comparing the χ^2_ν values, the Bayesian evidence, and the model parameters – but it is clear that it is still not a complete description of systems with asymmetric light curves. This is evidenced by, for example, the model favouring an edge-on inclination for J1227 in all situations despite strong penalties from priors. Further to this, for both sources the residuals in the u_s-band show systematic variations, implying that some aspects of the light curves are not captured by the model. The per-band residuals for the best-fitting hotspot model of J1023 are shown in Fig. 11. Examining these in more detail we find the model produces too much asymmetry in the u_s-band compared to the data, while for the i_s and g_s -bands the residuals show that the model is capturing the asymmetry well. Why this happens is not immediately clear. While it may be interpreted as further evidence that the hotspot model is insufficient, similar systematics are also present in the best-fitting heat redistribution model.

As is described in Section 4.4, our heat redistribution model incorporates the effects of diffusion and convection in the companion photosphere. Our results using this model are of comparable quality to the hotspot model, the Bayesian evidence indicating an improved fit over the direct heating model. However, the temperature distributions obtained differ significantly from those in the hotspot model, for example, for J1023 for which the polar spot disappears in the heat redistribution model. The temperature distribution of the best-fitting heat redistribution model is shown in Fig. 12. A possible model not tested in this work may be a combination of the two models; a hotspot with heat redistribution.

6.3 J1227

Despite the modelling failing to provide a single best-fitting solution, we can discuss several key findings. Our inclination range of $i \sim 50°$–$70°$ obtained by fitting at fixed inclinations agrees with the range proposed in de Martino et al. (2014) and de Martino et al. (2015), though these do not translate into a particularly strong mass

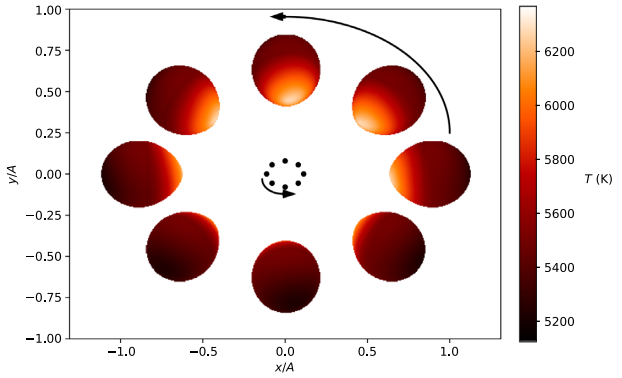

Figure 12. Companion star temperature distribution for the best-fitting heat redistribution (HR1) model of J1023. The asymmetry of this distribution can be seen near the L1 point, and the lack of the polar spot seen in the hotspot model is no longer present. The model light curve and residuals are indistinguishable from the hotspot case.

constraint: a pulsar mass in the range $M_p \sim 1.09$–2.0 M$_\odot$ and a companion mass in the range $M_c \sim 0.2$–0.37 M$_\odot$. However, the tendency of the model towards edge-on inclinations is concerning.

The lack of observed X-ray eclipses and the fact that no eclipse is observed in the spectra argue against this edge-on inclination. The preference for a high inclination in the model suggests that the model is attempting to increase the fraction of ellipsoidal modulation relative to the irradiation. The amplitude of the ellipsoidal modulation is also proportional to the filling factor cubed,

$$A_{\rm el} \sim f^3 q \sin^2 i, \tag{5}$$

while the irradiation amplitude is proportional to the square of the filling factor (Breton et al. 2012). The high inclination may be compensating for a smaller filling factor, which may be caused by the model attempting to fit the asymmetries with a larger ellipsoidal term than is truly present. The source of asymmetry in the system is still uncertain, while the two proposed model extensions do offer a significantly improved fit the discrepancies between the model parameters and observables, notably the inclination, suggest that there is still significant physics in the system that is not understood.

Before performing the modelling with fixed inclination described in Section 5.1.6, we attempted to model the system with the pulsar mass fixed over a range of values, as with J1023. However, the K_2 velocities obtained with these models were unacceptably large: more than three standard deviations above the spectroscopic distances. While we might expect some systematic error in this spectroscopic value, it cannot be large enough to explain this discrepancy. Since in these fixed-mass models the mass ratio and inclination are derived from K_2, the high inclinations that the model consistently prefers necessitate high-K_2 velocities. With the inclination fixed, q and $M_{\rm psr}$ are derived so this is no longer an issue and the model is well-behaved.

6.4 J1023

While several system parameters – namely the inclination, mass ratio, radial velocity, and filling factor – are broadly similar across the different models, some considerable differences remain. The temperature distributions and pulsar masses were starkly different in each case. Comparing the temperature distributions of the companion surfaces of each model, we see that the large polar spot seen on the hotspot model is not reproduced by the heat redistribution model, despite both models having very similar fit residuals. This could suggest that the large spot may be a sign of overfitting, which would indicate that the magnetic ducting theory proposed in Kandel et al. (2020) is not appropriate here. However, many CVs and rotating stars also display polar spots (Watson et al. 2007), which may suggest that the similar alignment of magnetic fields is not coincidental. It should be noted that the spots in Watson et al. (2007) are cold spots, as opposed to the hot spots which are favoured in this work. An additional explanation may be drawn from the fact that the viewing angle of this polar spot does not change much over the orbit, suggesting that this spot configuration is in fact fitting for an additional constant source of flux.

As such, we introduce a power law with an index of unity in order to mimic a third light in the system similar to what is observed in the AP state from broad-band spectroscopy (Hernandez Santisebastien et al., private communication). This light is incorporated as a fraction, t, of the expected flux from the companion alone such that $t = F_{\rm 3rd\,light}/F_{\rm companion}$. For each band, these correspond to $t_i = 0.150$, $t_g = 0.196$, and $t_u = 0.625$, with the contribution from the third light most significant in the u_s-band. We then adjust the fluxes prior to fitting by multiplying each band by the ratio $1/(1 + t)$ such that the modelled contribution of the third light is removed and the remaining flux represents only the light from the companion. We use a heat redistribution model with linear diffusion and constant advection profile. We chose this model over the better-fitting hotspot model as for that model the free temperature of the spot makes it difficult to clearly separate the flux contributions of each source. That is, the spot temperature can easily decrease to compensate for the reduced flux.

While the adjusted i_s and g_s-bands were fit well by the model, the adjusted flux of the u_s-band could not be matched. This suggests that either our power-law model does not accurately describe the third light flux, or that a third light is not able to account for the distance discrepancy. Notably, the shape of the residuals in u' were unchanged compared to a fit using unaltered fluxes. We note that the spectra presented in Shahbaz et al. (2019) show no evidence for a stellar third light. A continuum emission source such as the synchrotron emission produced in the intrabinary shock (Romani & Sanchez 2016) may be an alternative source of the flux; however, this emission follows a negative power law. Shahbaz et al. (in preparation and private communication) further show no evidence for a third light, with the secondary star the sole source of flux from 6000 Å. However, a metal-rich secondary is observed with an iron excess of Fe/H = 0.48 (Shahbaz et al. 2019 and private communication). This results in a u'-band flux of 82 per cent the solar equivalent in our model, which may account for the closer distance that we obtain due to excess flux: a metal rich star is less blue compared to solar. A system distance of between 1.25 and 1.30 kpc, as we obtain, compared to the interferometry distance of 1.368 kpc corresponds with a decrease in magnitude of between 0.11 and 0.2 mag in the u_s-band. This is equivalent to a decrease in flux of 83–90 per cent, which is comparable to the expected decrease due to a higher metallicity. The atmosphere grids used in this modelling do not account for this high iron excess, and as such this avenue may help to explain the distance we obtain.

While the best-fitting values are different for the heat redistribution and hotspot models, both show a strong covariance between the filling factor, f, and the distance. This can be seen in the corner plot shown in Fig. 13. This suggests that a better fit to the distance will bring the filling factor closer to unity, as we would initially expect.

Considering the competing prior values for the A_V extinction, our modelling shows that both values are almost equally favoured as no other parameters are affected by the change of prior within uncertainties. As such, we can surmise that the small difference in

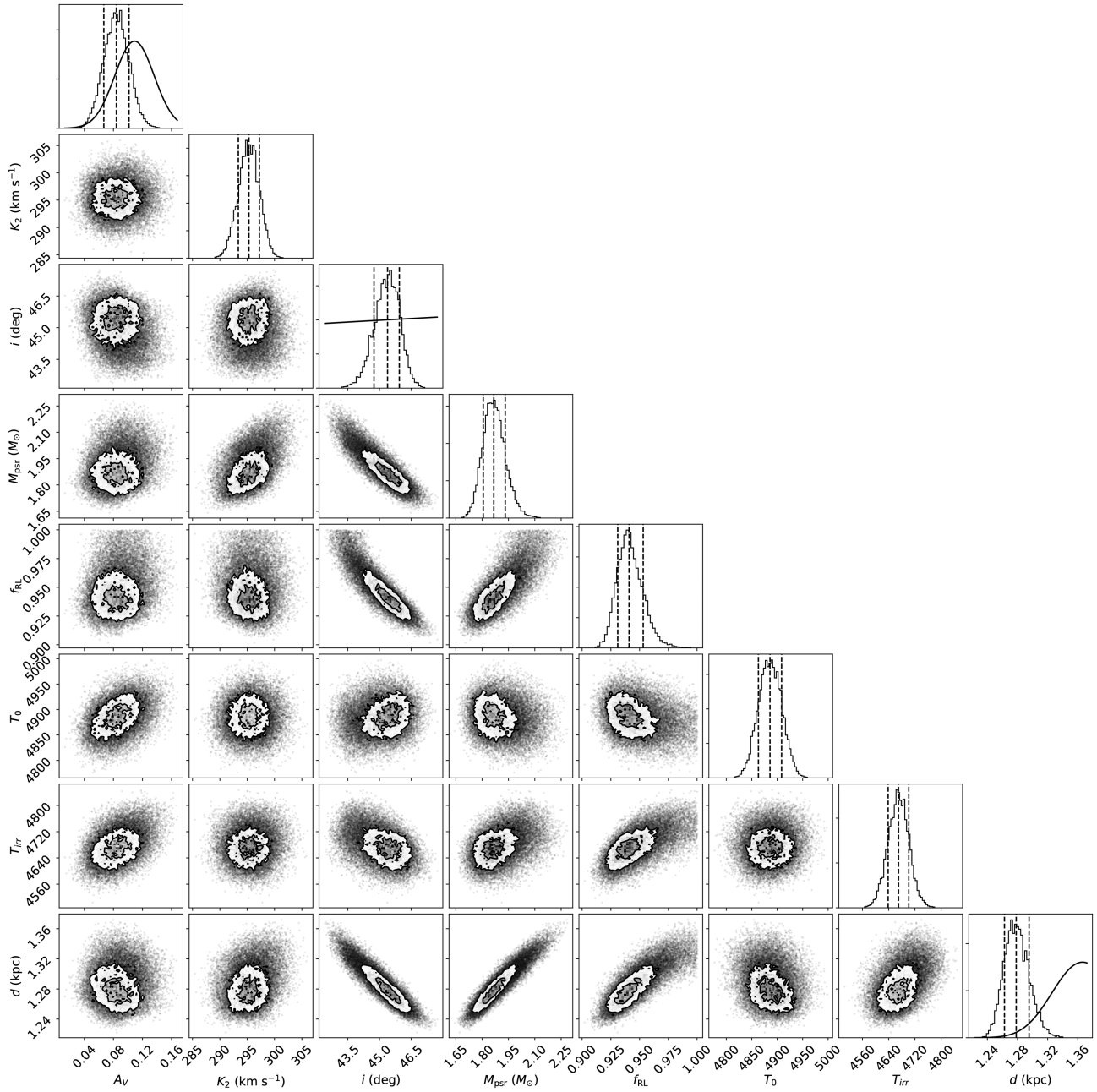

Figure 13. Corner plot of selected parameters of the J1023 hotspot model. Not shown are the hotspot parameters and the mass ratio. Note the discrepancy between the distance posterior and prior distribution, and the strong covariance of the distance with the inclination, pulsar mass, and filling factor.

model evidence (-2297.1 for the value from N_H and -2293.9 for the A_V from dust maps) are due only to the differences in penalty from the A_V priors. The A_V value from the dust maps, which provides the marginally improved model evidence, was used for the modelling in this work though, in practice, this investigation shows that the model parameter posteriors are nearly ideally distributed and any changes to the A_V have little effect on the results.

7 CONCLUSIONS

We present new high-time resolution optical photometry of the tMSPs PSR J1023+0038 and PSR J1227−4853, and discuss our numerical modelling of their light curves. Using a new extension to the ICARUS code including the thermal contributions of a hot or cold spot on the companion surface, we modelled the asymmetric light curves of these sources and obtained significantly improved fits over the symmetric case. Using this model we constrained several key parameters of the systems, including the companion RL filling factor, temperature profile, and system distance. We also performed modelling using a further extension which considers the diffusion and convection on the companion star surface. This model also provided an improved fit compared to the symmetric model, though for both systems the evidence favours a model with a hotspot.

We found that the filling factor of both sources was less than 1.0, indicating that the RL is underfilled. This is at odds with other results showing a full RL in the system's RP state (de Martino et al. 2014).

We expect the companion in the AP state to fill its RL, so these results indicate that the filling factor plays an important role in the tMSP transition. However, when considering the volume-averaged filling factor, we find that the companion stars are only slightly underfilling their RLs. Our results suggest that the companion stars may undergo an expansion and contraction between the AP and RP states of tMSP cycle, as there is no sign of a change in the size of the RL; changes in the orbital period are not large enough to account for the under full RL. Taking our filling factors at face value, they indicate that between state transitions the stellar radius changes by an order or 5 per cent, something which may be possible if the companion has a core-envelope structure with only a small fraction of its mass in the envelope.

Some of the limitations and errors in our results indicate that our model does not completely describe the asymmetry of the light curves, suggesting that improvements to the model are needed, or indeed a new physically motivated approach. For example, significant systematics remain in the residuals of the u_s-band of J1023. Using a further extension to the ICARUS code which models diffusion and convection in the companion photosphere, we performed a second round of modelling. This again provided an improved fit over the symmetric model; however, the inconsistent results such as the inclination of J1227, persisted, and indeed the fit overall was poorer than the hotspot case. However, modelling with some combination of the two extensions may be a good starting point or future investigations.

Even with these excellent data, these sources are not ideally modelled. Despite this, we believe the integrity of the key findings are intact and recommend additional study of these two systems. In particular for J1227, additional spectroscopy and radio interferometry would significantly improve the constraints on the distance and inclination.

ACKNOWLEDGEMENTS

JGS, RPB, CJC, GV, MRK, and DMS acknowledge the support of the European Research Council, under the European Union's Horizon 2020 research and innovation program (grant agreement No. 715051; Spiders). VSD and TM acknowledge the support of the Science and Technology Facilities Council (STFC), grant number ST/T000406/1. TS thanks the Spanish Ministry of Economy and Competitiveness (MINECO; grant AYA2017-83216). This work has made use of data from the European Space Agency (ESA) mission *Gaia* (https://www.cosmos.esa.int/gaia), processed by the *Gaia* Data Processing and Analysis Consortium (DPAC; https://www.cosmos.esa.int/web/gaia/dpac/consortium). Funding for the DPAC has been provided by national institutions, in particular the institutions participating in the *Gaia* Multilateral Agreement.

Lastly, this work has made extensive use of the PYTHON language, including the ASTROPY (Astropy Collaboration 2013), MATPLOTLIB (Hunter 2007), NUMPY (van der Walt, Colbert & Varoquaux 2011), and SCIPY (Virtanen et al. 2020) packages.

DATA AVAILABILITY

The ULTRACAM light curves are available in Zenodo (10.5281/zenodo.4680510). The raw ULTRACAM images are available upon request.

REFERENCES

Alpar M. A., Cheng A. F., Ruderman M. A., Shaham J., 1982, Nature, 300, 728
Ambrosino F. et al., 2017, Nature Astron., 1, 854
Archibald A. M. et al., 2009, Science, 324, 1411
Archibald A. M., Kaspi V. M., Hessels J. W. T., Stappers B., Janssen G., Lyne A., 2013, preprint (arXiv:1311.5161)
Astropy Collaboration, 2013, A&A, 558, A33
Baglio M. C. et al., 2019, A&A, 631, A104
Bassa C. G. et al., 2014, MNRAS, 441, 1825
Bogdanov S., Patruno A., Archibald A. M., Bassa C., Hessels J. W. T., Janssen G. H., Stappers B. W., 2014, ApJ, 789, 40
Bogdanov S. et al., 2015, ApJ, 806, 148
Bogdanov S. et al., 2018, ApJ, 856, 54
Bonazzola S., Gourgoulhon E., Marck J.-A., 1999, Journal of Computational and Applied Mathematics, 109, 433
Bond H. E., White R. L., Becker R. H., O'Brien M. S., 2002, PASP, 114, 1359
Bonnet-Bidaud J. M., de Martino D., Mouchet M., Falanga M., Belloni T., Masetti N., Mukai K., Matt G., 2012, Mem. Soc. Astron. Ital., 83, 742
Breton R. P., Rappaport S. A., van Kerkwijk M. H., Carter J. A., 2012, ApJ, 748, 115
Breton R. P. et al., 2013, ApJ, 769, 108
Britt C. T., Strader J., Chomiuk L., Tremou E., Peacock M., Halpern J., Salinas R., 2017, ApJ, 849, 21
Buchner J. et al., 2014, A&A, 564, A125
Cardelli J. A., Clayton G. C., Mathis J. S., 1989, ApJ, 345, 245
Castelli F., Kurucz R. L., 2003, in Piskunov N., Weiss W. W., Gray D. F., eds, Proc. IAU Symp. 210, Modelling of Stellar Atmospheres, Poster Contributions. Uppsala University, Uppsala, Sweden, p. A20
Chen H.-L., Chen X., Tauris T. M., Han Z., 2013, ApJ, 775, 27
Clark C. J. et al., 2021, MNRAS, 502, 915
Coti Zelati F. et al., 2014, MNRAS, 444, 1783
Coti Zelati F. et al., 2019, A&A, 622, A211
Cumming A., Zweibel E., Bildsten L., 2001, ApJ, 557, 958
De Falco V., Kuiper L., Bozzo E., Ferrigno C., Poutanen J., Stella L., Falanga M., 2017, A&A, 603, A16
de Martino D. et al., 2010, A&A, 515, A25
de Martino D. et al., 2013, A&A, 550, A89
de Martino D. et al., 2014, MNRAS, 444, 3004
de Martino D. et al., 2015, MNRAS, 454, 2190
de Wit J., Gillon M., Demory B. O., Seager S., 2012, A&A, 548, A128
Deller A. T. et al., 2012, ApJ, 756, L25
Deller A. T. et al., 2015, ApJ, 809, 13
Demory B.-O. et al., 2013, ApJ, 776, L25
Dhillon V. S. et al., 2007, MNRAS, 378, 825
Dhillon V. et al., 2018, in Evans C. J., Simard L., Takami H., eds, Proc. SPIE Conf. Ser. Vol. 10702, Ground-based and Airborne Instrumentation for Astronomy VII. SPIE, Bellingham, p. 107020L
Eggleton P. P., 1983, ApJ, 268, 368
Feroz F., Hobson M. P., Bridges M., 2009, MNRAS, 398, 1601
Green G. M. et al., 2018, MNRAS, 478, 651
Honeycutt R. K., 1992, PASP, 104, 435
Hunter J. D., 2007, Comput. Sci. Eng., 9, 90
Jackson B., Adams E., Sandidge W., Kreyche S., Briggs J., 2019, AJ, 157, 239
Jaodand A., Archibald A. M., Hessels J. W. T., Bogdanov S., D'Angelo C. R., Patruno A. r., Bassa C., Deller A. T., 2016, ApJ, 830, 122
Jaodand A. D. et al., 2021, preprint (arXiv:2102.13145)
Johnson T. J. et al., 2015, ApJ, 806, 91
Kandel D., Romani R. W., 2020, ApJ, 892, 101
Kandel D., Romani R. W., Filippenko A. V., Brink T. G., Zheng W., 2020, ApJ, 903, 39
Kennedy M. R., Clark C. J., Voisin G., Breton R. P., 2018, MNRAS, 477, 1120
Kennedy M. R. et al., 2020, MNRAS, 494, 3912

Kippenhahn R., Weigert A., Weiss A., 2012, Stellar Structure and Evolution. Springer, Berlin
Komacek T. D., Showman A. P., 2020, ApJ, 888, 2
Konar S., Bhattacharya D., 1997, MNRAS, 284, 311
Levin L. et al., 2013, MNRAS, 434, 1387
Li M., Halpern J. P., Thorstensen J. R., 2014, ApJ, 795, 115
Linares M., 2014, ApJ, 795, 72
Linares M., 2020, in Multifrequency Behaviour of High Energy Cosmic Sources - XIII. Available at https://pos.sissa.it/cgi-bin/reader/conf.cgi?confid=362
Lucy L. B., 1967, ZAp, 65, 89
Luri X. et al., 2018, A&A, 616, A9
Martin T. J., Davey S. C., 1995, MNRAS, 275, 31
McConnell O., Callanan P. J., Kennedy M., Hurley D., Garnavich P., Menzies J., 2015, MNRAS, 451, 3468
Nieder L. et al., 2020, ApJ, 902, L46
Olver F. W. J., Lozier D., Boisvert R., Clark C., 2010, NIST Handbook of Mathematical Functions. Cambridge Univ. Press, New York
Papitto A. et al., 2013, Nature, 501, 517
Papitto A. et al., 2018, ApJ, 858, L12
Papitto A. et al., 2019, ApJ, 882, 104
Patruno A. et al., 2014, ApJ, 781, L3
Roberts M. S. E., 2011, in Burgay M., D'Amico N., Esposito P., Pellizzoni A., Possenti A., eds, AIP Conf. Proc. Vol. 1357, New Black Widows and Redbacks in the Galactic Field. Am. Inst. Phys., New York, 127
Romani R. W., Sanchez N., 2016, ApJ, 828, 7
Romani R. W., Kandel D., Filippenko A. V., Brink T. G., Zheng W., 2021, ApJ, 908, L46
Roy J. et al., 2015, ApJ, 800, L12
Schaffenroth V. et al., 2019, A&A, 630, A80
Schlafly E. F., Finkbeiner D. P., 2011, ApJ, 737, 103
Schroeder J., Halpern J., 2014, ApJ, 793, 78
Shahbaz T. et al., 2015, MNRAS, 453, 3461
Shahbaz T., Linares M., Breton R. P., 2017, MNRAS, 472, 4287
Shahbaz T., Dallilar Y., Garner A., Eikenberry S., Veledina A., Gandhi P., 2018, MNRAS, 477, 566
Shahbaz T., Linares M., Rodríguez-Gil P., Casares J., 2019, MNRAS, 488, 198
Soker N., 2015, ApJ, 800, 114
Stappers B. W. et al., 2014, ApJ, 790, 39
Strader J., Li K.-L., Chomiuk L., Heinke C. O., Udalski A., Peacock M., Shishkovsky L., Tremou E., 2016, ApJ, 831, 89
Takata J. et al., 2014, ApJ, 785, 131
Thorstensen J. R., Armstrong E., 2005, AJ, 130, 759
van der Walt S., Colbert S. C., Varoquaux G., 2011, Comput. Sci. Eng., 13, 22
Virtanen P. et al., 2020, Nat. Methods, 17, 261
Voisin G., Kennedy M. R., Breton R. P., Clark C. J., Mata-Sánchez D., 2020, MNRAS, 499, 1758
Wade R. A., Horne K., 1988, ApJ, 324, 411
Wang Z., Archibald A. M., Thorstensen J. R., Kaspi V. M., Lorimer D. R., Stairs I., Ransom S. M., 2009, ApJ, 703, 2017
Watson C. A., Steeghs D., Shahbaz T., Dhillon V. S., 2007, MNRAS, 382, 1105
Wieczorek M. A., Meschede M., 2018, Geochem. Geophys. Geosystems, 19, 2574
Woudt P. A., Warner B., Pretorius M. L., 2004, MNRAS, 351, 1015
Zilles A., Kotera K., Rohrmann R., Althaus L., 2020, MNRAS, 492, 1579

APPENDIX A: ICARUS MODEL EXTENSIONS

A1 Hot spot model

For the hotspot model, we consider the spot temperature, $T_{\rm spot}$, the spot radius, $R_{\rm spot}$, and the spot position angles, θ_s, ϕ_s. θ, and ϕ are the polar angle and azimuth angle such that $\theta_s = 0^\circ$ is the North pole of the companion and $\phi_s = 90^\circ$ is the direction towards the L1 point. The spot temperature is added to the base temperature of the companion after the effects of gravity darkening but before the irradiation such that $T_{\rm star}(\theta_s, \phi_s)^4 = (T_0 + T_{\rm spot}(\theta_s, \phi_s))^4 + T_{\rm irr}(\theta_s, \phi_s)^4$. In practice, there is little difference between this configuration and applying the spot after the irradiation; only the width of the spot would change. The spot geometry is defined by a 2D, axially symmetric Gaussian profile with a central maximum temperature of $T_{\rm spot}$ and width of $R_{\rm spot}$, with $R_{\rm spot} < 90^\circ$.

A2 Heat redistribution model

Energy transport follows the model (Voisin et al. 2020),

$$\nabla_\parallel \cdot \boldsymbol{J}_\parallel = -\left(\sigma_{\rm sb}\left(T_*^4 - T_0^4\right) - L_{\rm w}\right), \tag{A1}$$

which reduces to direct heating when the right-hand side is zero, and

$$\boldsymbol{J}_\parallel = -\kappa\left(\frac{T_*}{T_{\rm max}}\right)^\Gamma \nabla_\parallel T_* - T_* f(\theta)\sin(\theta)\boldsymbol{u}_\phi, \tag{A2}$$

which is a generalization of the parallel energy transport law derived in Voisin et al. (2020; see appendix B). $\mathbf{J}_\parallel$ is the surface energy flux, $\nabla_\parallel$ is the 'surface gradient', κ is the diffusion coefficient, T_* is the surface temperature of the companion, Γ is the diffusion index, $f(\theta)$ is the polar convection profile, and $\mathbf{u}_\phi$ is the unit vector of the longitude. $T_{\rm max}$ is an arbitrary constant, which we define as $T_{\rm max}^4 = T_{\rm day}^4 = T_0^4 + T_{\rm irr}^4$. For this extension to the model, note that the spherical coordinates are defined differently to those in the hotspot model. θ is the colatitude, with the spherical coordinates defined such that the polar axis is the spin axis of the star, with $\phi = 0$ intersecting the binary axis on the night side of the star.

Out of several forms of polar convection profile, $f(\theta)$, we initially chose $f(\theta) = v$, where v is the strength of the convection current in energy flux per unit temperature and is the first additional model parameter. This profile describes constant longitudinal advection. We also chose a convection profile of the form $f(\theta) = v\exp(-\frac{\theta^2}{2w^2})$, which localizes this flow to a Gaussian region around the equator with angular width w. We allow for the diffusion coefficient $\kappa(\frac{T_*}{T_{\rm max}})^\Gamma$ to depend on the local temperature following a power law of index Γ.

APPENDIX B: HEAT REDISTRIBUTION WITH TEMPERATURE-DEPENDENT DIFFUSION LAW

B1 Diffusion law and equation of energy redistribution

In Voisin et al. (2020), it is only described the case of the constant diffusion coefficient κ. In the present paper, we make use of a conceptually straightforward generalization of this work by introducing a temperature-dependant diffusion coefficient, whereby $\kappa \rightarrow \kappa(T) = \kappa_{\rm max}(T/T_{\rm max})^\Gamma$ as shown in equation (A2). For clarity and simplicity we use here $T \equiv T_*$, and the constant coefficient κ of equation (A2) is here written $\kappa_{\rm max}$.

In this case, $\kappa_{\rm max}$ is the value of the temperature-dependent coefficient at $T = T_{\rm max}$, and Γ is the diffusion power-law index. Scaling the temperature by a 'maximum' temperature $T_{\rm max}$ allows us to decorrelate the effect of variation of the diffusion index Γ from variations of $\kappa_{\rm max}$. The choice of $T_{\rm max}$ is somewhat arbitrary (but should be such that $0 < T/T_{\rm max} \lesssim 1$ for the reason mentioned above). It is convenient to define

$$T_{\rm max} = \left(T_0^4 + \bar{T}_{\rm ir}^4\right)^{1/4}, \tag{B1}$$

where T_0 is the base temperature of the star, $L_w(a) = \sigma_{\rm sb}\bar{T}_{\rm ir}^4$, $L_w(a)$ being the wind flux at the separation distance a, and $\sigma_{\rm sb}$ the Stefan–

Boltzmann constant. In the case of direct heating of a spherical star at homogeneous surface temperature by a spherically symmetric pulsar wind, this is indeed the maximum temperature at the surface of the companion star.

The equation of energy redistribution, equation (A1), now becomes

$$\nabla_\parallel \cdot \left(\kappa(T)\nabla_\parallel T\right) + f(\theta)\partial_\phi T = \sigma_{\rm sb}\left(T^4 - T_0^4\right) - L_{\rm w}, \tag{B2}$$

where the diffusion term can be expanded as

$$\nabla_\parallel \cdot \left(\kappa(T)\nabla_\parallel T\right) = \kappa_{\rm max}\left[\left(\frac{T}{T_{\rm max}}\right)^\Gamma \nabla_\parallel^2 T + \left(\frac{T}{T_{\rm max}}\right)^{\Gamma-1}\frac{\left(\nabla_\parallel T\right)^2}{T_{\rm max}}\right]. \tag{B3}$$

B2 Linearization and numerical solution

In Voisin et al. (2020) is explained how the redistribution equation can be solved iteratively as the limit of the sequence

$$T_{n+1} = T_n + t_{n+1}, \tag{B4}$$

where t_{n+1} is the solution of equation (B2) linearized with respect to T_n, and $T_0 = T_{\rm dh}$; $t_0 = 0$ initialize the sequence.

In the present case, this scheme appears to diverge when $\Gamma \neq 0$ and $\kappa_{\rm max}$ is sufficiently large, typically when $t_1 \gtrsim T_b$. However, we found that a solution can be computed for any reasonable $\kappa_{\rm max}$ and Γ by first computing the $\Gamma = 0$ solution (with the desired $\kappa_{\rm max}$) using the above scheme, and subsequently computing the sought solution by substituting $T_{\rm dh}$ by the $\Gamma = 0$ solution as the initial condition of a new iteration.

The linearized equation (B2) can be cast in the form:

$$\left(A_n - B_n - f(\theta)\partial_\phi\right) t_{n+1} = S_n, \tag{B5}$$

with

$$A_n = 4\sigma_{\rm sb}T_n^3, \tag{B6}$$

$$S_n = S_n^{\rm (dif)} + f(\theta)\partial_\phi T_n - \sigma\left(T_n^4 - T_0^4\right) + L_{\rm w}. \tag{B7}$$

The difference with equations (A10)–(A12) of Voisin et al. (2020) lies in the diffusion operator B_n and source $S_n^{\rm (dif)}$. These are obtained by linearising equation (B3) around T_n,

$$\nabla_\parallel \cdot \left(\kappa(T_{n+1})\nabla_\parallel T_{n+1}\right) = B_n t_{n+1} + S_n^{\rm (dif)} + \bigcirc\left(t_{n+1}^2\right), \tag{B8}$$

where,

$$B_n = \kappa' T_n^{\Gamma-2}\left[T_n^2\nabla_\parallel^2 + 2\Gamma T_n\nabla_\parallel T_n\cdot\nabla_\parallel + \Gamma T_n\nabla_\parallel^2 T_n + \Gamma(\Gamma-1)\left(\nabla_\parallel T_n\right)^2\right], \tag{B9}$$

$$S_n^{\rm (dif)} = \kappa' T_n^{\Gamma-1}\left[T_n\nabla_\parallel^2 T_n + \Gamma\left(\nabla_\parallel T_n\right)^2\right], \tag{B10}$$

where for simplicity with have noted $\kappa' \equiv \kappa_{\rm max}/T_{\rm max}^k$.

As explained in Voisin et al. (2020), equation (B5) can be solved algebraically by decomposing t_{n+1} on the basis of spherical harmonics. Numerically, this can be done using publicly available tools such as SHTOOLS (Wieczorek & Meschede 2018).[2]

The solution is then obtained using spectral methods (e.g. Bonazzola, Gourgoulhon & Marck 1998): in the space of spherical harmonics multiplication by a function and derivatives become matrix operators (truncated to the desired order). In particular, multiplication by a function $g(\theta, \phi)$ is given by a matrix of components

$$M_{ij}^\times = \sum_k g_k \mu_{ijk}, \tag{B11}$$

where g_k are the components of the spherical harmonics decomposition of g and μ is such that

$$Y_\beta Y_\gamma = \sum_\alpha Y_\alpha \mu_{\alpha\beta\gamma}, \tag{B12}$$

where Y_γ are the set of spherical harmonics.

With complex spherical harmonics, the derivative with respect to ϕ is given by

$$M_{ab}^{\partial_\phi} = i m_a \delta_{ab}, \tag{B13}$$

where $\delta_{ab} = 1$ if $a = b$ and 0 otherwise, m_a is the spherical harmonic degree corresponding to index a and $i^2 = -1$.

In order to calculate the θ derivative, we use the recurrence relation of associated Legendre functions Olver & National Institute of Standards and Technology (U.S.; 2010),

$$\frac{{\rm d}P_l^m}{{\rm d}\theta}(\cos\theta) = \frac{1}{\sin\theta}\left[(l+1-m)P_{l+1}^m(\cos\theta) - (l+1)\cos\theta\, P_l^m(\cos\theta)\right], \tag{B14}$$

in order to decompose numerically each $\partial_\theta Y_l^m$ on to the basis of spherical harmonics and thus obtain the matrix M^{∂_θ}.

It follows that, for example, $g(\theta, \phi)\partial_\phi$ translates into $M^\times M^{\partial_\phi}$ in spherical harmonic space.

[2] https://shtools.github.io/SHTOOLS/

This paper has been typeset from a TEX/LATEX file prepared by the author.